Available online at www.sciencedirect.com
ScienceDirect
Journal of Volcanology and Geothermal Research 169 (2008) 121–144
Journal of volcanology and geothermal research
www.elsevier.com/locate/jvolgeores

Research paper

Welded block and ash flow deposits from Mount Meager, British Columbia, Canada

K.A. Michol, J.K. Russell *, G.D.M. Andrews

Volcanology & Petrology Laboratory, Department of Earth & Ocean Sciences, University of British Columbia, Vancouver, British Columbia, Canada V6T 1Z4

Received 4 April 2007; accepted 22 August 2007
Available online 31 August 2007

Abstract

The 2360 years B.P. eruption of Mount Meager, British Columbia, produced a succession of rarely observed, welded block and ash flow deposits and non-welded equivalents. We report on these rhyodacitic block and ash flow deposits by describing the deposits, documenting the nature of the welding process, and establishing the origins of these pyroclastic deposits. Variations in welding intensity are tracked by image analysis of field texture maps, petrographic study of shard morphology, and measurements of sample density and porosity. Pyroclast oblateness from image analysis of texture maps provides a qualitative record of welding intensity, but underestimates the amount of compactional (*e.g.*, volume) strain when compared to estimates from physical property measurements (*e.g.*, density, porosity). Unconsolidated deposits have an average matrix porosity of ~ 41% (38–45%) and clasts have an average porosity of ~ 32% (24–40%). In unconsolidated deposits, isolated porosity is pervasive (< 8%) in juvenile clasts, but is near absent in samples of matrix (< 1%). Welding and compaction cause a reduction in both connected and isolated porosity. Clasts and matrix record equivalent amounts of strain (~ 38%) and, thus, are fully coupled during the welding and compaction process. The average integrated strain for vertical sections of the deposit is 31% implying > 50 m shortening of the thickest deposit (from 162 m to the current 112 m). The pyroclastic flow deposits result from accumulation in a narrow, confined river valley; the accumulation was sufficiently rapid to keep the deposits above their glass transition temperature thereby allowing the succession to weld as a single cooling unit. The nature and distribution of isolated porosity in the juvenile clasts of rhyodacite suggest an explosive (rather than effusive) origin for these block and ash flow deposits that may be analogous to some Vulcanian-eruption-triggered dome-collapse processes observed at Soufrière Hills Volcano, Montserrat (rather than gravitational collapse).

Keywords: pyroclastic; block and ash flow deposit; welding; strain; density; porosity

1. Introduction

Block and ash flows, also known as nuées ardentes, are small-volume pyroclastic density currents (generally less than 1 km^3) generated by the explosive or gravitational collapse of lava flows or domes (*e.g.*, Miyabuchi, 1999). Block and ash flow deposits are topographically controlled, unsorted deposits having an ash-rich matrix and a near-monolithologic assemblage of moderately to poorly vesiculated clasts (porosity (Φ) < 45%). Deposits typically show crude reverse grading and lava blocks showing radially oriented cooling joints can be common (*e.g.*, Stewart et al., 2003). Classic examples include deposits from Merapi (Bardintzeff,

* Corresponding author. Tel.: +1 604 822 2703; fax: +1 604 822 6088.
E-mail address: krussell@eos.ubc.ca (J.K. Russell).

0377-0273/$ - see front matter © 2007 Elsevier B.V. All rights reserved.
doi:10.1016/j.jvolgeores.2007.08.010

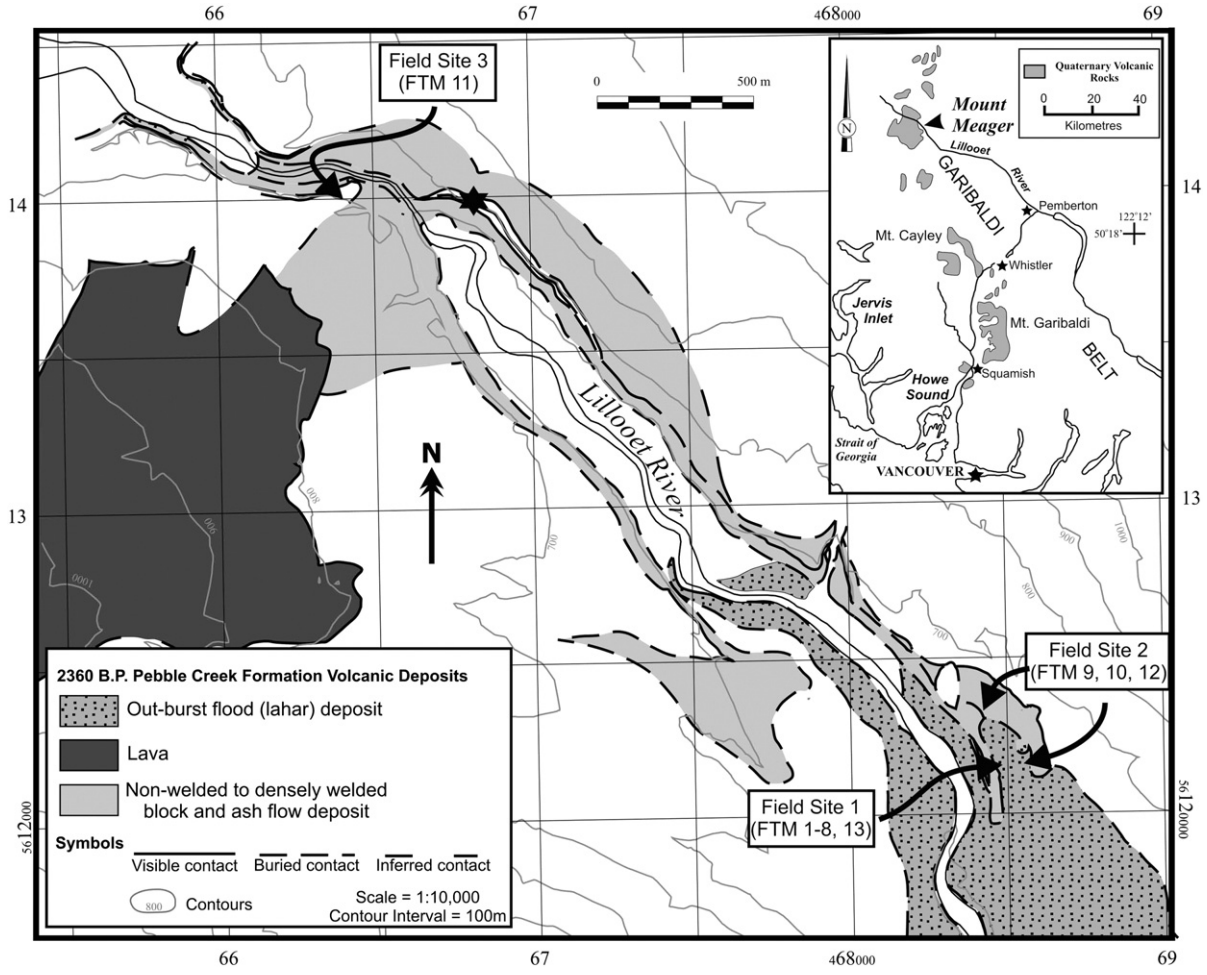

Fig. 1. Geological map showing distributions of deposits resulting from 2360 B.P. eruption of Mount Meager (modified from Stewart, 2002). Locations of field sites and field texture maps (FTMs) are also shown. Inset shows geographic location of Mount Meager within southwest British Columbia.

1984; Boudon et al., 1993; Abdurachman et al., 2000), Unzen (Sato et al., 1992; Ui et al., 1999), and Montserrat (Calder et al., 2002; Woods et al., 2002). They differ from pumiceous pyroclastic density currents and their deposits in that ignimbrites generally contain higher fractions of ash, and the lapilli and block-sized clasts are pumiceous (Φ>50%) (Branney and Kokelaar, 2002).

Welding of block and ash pyroclastic flow deposits is rare; for example, Cas and Wright (1987, p.111) state that there are no documented occurrences. Here, we report on a sequence of welded block and ash flow deposits at Mount Meager, southwestern British Columbia (Fig. 1). Our purpose is threefold: (1) to describe the physical attributes of the block and ash flow deposits; (2) to document the changes in texture and physical properties from non-welded to welded facies; and (3) to use these observations to explore the origins of these unique welded pyroclastic deposits.

2. Mount Meager volcanic complex

The Mount Meager Volcanic Complex is part of the Garibaldi Volcanic Belt, the northernmost segment of the Cascade Volcanic Belt (Green et al., 1988; Read, 1990; Sherrod and Smith, 1990; Green and Sinha, 2005) (Fig. 1). This calc–alkaline composite stratovolcano rises to an elevation of 2645 m and overlies basement rocks of the southern Coast Belt. Volcanism at this complex ranges from 2.2 Ma (K–Ar) to its most recent explosive eruption 2360 (calendar years) B.P. (Nasmith et al., 1967; Read, 1977, 1979, 1990; Clague et al., 1995).

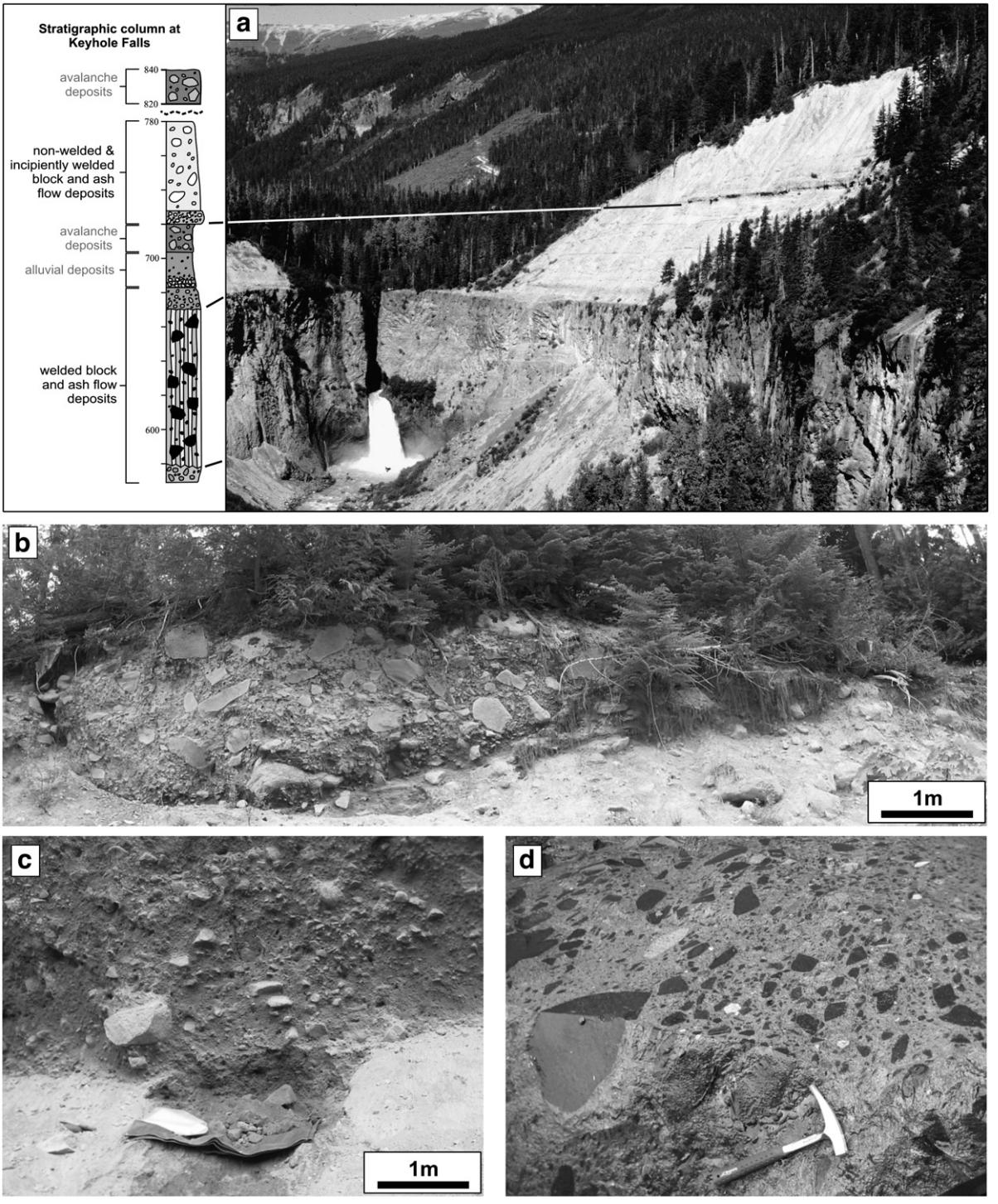

Fig. 2. Photographs illustrating lithostratigraphic facies variations within block and ash flow deposits of Pebble Creek formation. (a) Northwest-facing photograph showing deposits exposed at Keyhole Falls in Lillooet River valley and summarized in stratigraphic column. Lower cliff-forming unit comprises densely welded facies and is 100–115 m thick. Upper bedded units (above solid line) comprise interbedded fluvial gravels and non-welded to incipiently welded block and ash flow deposits. Section is capped by younger rock avalanche deposits. (b) Incipiently welded facies (oxidized) from the upper part of the succession (Field Site 2); (c) basal, non-welded facies (Field Site 1); and, (d) densely welded facies (Field Site 1).

2.1. Pebble Creek formation

The 2360 B.P. eruption (Nasmith et al., 1967; Clague et al., 1995) produced a sequence of rhyodacite volcaniclastic deposits and lava domes and flows that constitute the Pebble Creek Formation (Fig. 1; Stasiuk et al., 1996; Hickson et al., 1999; Stewart, 2002; Stewart et al., 2003). The vent is situated at 1500 m elevation, roughly 1000 m above the present stream bed of the Lillooet River and cuts through older volcanic deposits of the Plinth Assemblage (~ 90–100 ka; Read, 1979). The 2360 B.P. eruption began with a Plinian phase that generated pumice fall deposits and associated ignimbrites (Stasiuk et al., 1996; Hickson et al., 1999). The Plinian phase was followed by a less explosive phase that produced a sequence of block and ash flow deposits that accumulated mainly in the Lillooet River valley (Figs. 1, 2a). These deposits are the focus of this study. The eruption cycle ended with the extrusion of rhyodacite lava (Fig. 1). There is no evidence for a pronounced hiatus between individual events.

Many of the volcanic deposits from the 2360 B.P. eruption, the block and ash flow deposits in particular, accumulated in the paleo-Lillooet River valley and dammed the river upstream of Keyhole Falls (Figs. 1, 2; Hickson et al., 1999; Stewart, 2002). The dam produced an ephemeral lake that ultimately caused the failure of the dam and produced a hot lahar (Fig. 1; Hickson et al., 1999). The outburst flood event also excavated the large canyon that provides exposure of these welded breccias (Fig. 2a).

2.2. Block and ash flow deposits

The block and ash flow deposits of the Pebble Creek formation are mainly confined to a steep-sided canyon representing an earlier incarnation of the Lillooet River (Stasiuk et al., 1996; Hickson et al., 1999). The unit is approximately 175 m thick immediately below the inferred vent at the Keyhole Falls locality (Figs. 1, 2a), forms a wedge-shaped deposit that thins to < 25 m at 2.5 km downstream, and has an estimated volume of 0.2–0.25 km^3 (Stewart, 2002).

The block and ash flow deposits are dominantly monomict volcaniclastic breccias composed of centimetre- to metre-sized crystal-rich, rhyodacite obsidian clasts, supported by a porous, ash-sized matrix (Fig. 2b–d). Accidental, centimeter-sized, subangular to rounded, lithic clasts of monzonite and Plinth Assemblage volcanic rocks are pervasive but in low abundance. The deposits are dominantly massive and very poorly sorted (Fig. 2b–d). Cryptic reversely graded bedding is observed locally and defined by variations in maximum clast size. These are inferred to be block and ash flow deposits because of their: (1) poor sorting; (2) monolithologic juvenile clasts of rhyodacite lava; (3) ash-rich matrix; and (4) many features indicating a hot emplacement (see below). These characteristics parallel those of block and ash flow deposits reported from other classic examples (*e.g.*, Merapi, Unzen, and Montserrat).

2.3. Welding facies

The block and ash flow deposits range widely in welding intensity and four separate welding facies have been sampled from three field sites (Fig. 1; Table 1). These include: (1) non-welded facies from the base of the succession; (2) densely welded facies from the interior of the deposit; (3) oxidized and incipiently welded facies near the top of the sequence; and (4) non-welded facies from the top of the sequence.

The basal non-welded facies at Field Site 1 is a ~ 2-m-thick, unconsolidated, poorly sorted, massive volcaniclastic deposit featuring monolithologic lapilli and blocks of rhyodacite supported by a grey, ash matrix (Fig. 2c). Clasts are mostly subangular to subrounded, typically 5–15 cm in diameter, and rarely up to 1 m. Most juvenile clasts of rhyodacite are moderately vesicular ($\Phi \sim 30$–40%) although some blocks are much denser ($\Phi \sim 2$–5%). Rare accidental clasts of Plinth Assemblage rocks and monzonite country rock are present. The base of this deposit conformably overlies an earlier ignimbrite; the non-welded facies grades upwards into densely welded facies over an interval of ~ 2 m.

Field Site 1 was also used to study the densely welded facies. Above the non-welded base is a 16-m-

Table 1
Location and description of field sites, including associated field texture maps (FTMs; see Fig. 1)

Field site	Description	Facies	FTM #
1	Valley wall exposure in Lillooet River valley; cliff and fallen blocks	Densely welded (middle of deposit)	1–6
		Non-welded (base of deposit)	7, 8, 13
2	Roadcut exposure ~ 300 m NE of Field Site 1	Incipiently welded (upper oxidized section)	9, 10, 12
3	Roadcut exposure on south side of bridge at Keyhole Falls	Non-welded (upper non-oxidized section)	11

thick, highly indurated, poorly sorted, weakly foliated, vitroclastic breccia (Fig. 2d). The deposit features angular to subrounded, dense, black, glassy clasts of rhyodacite supported by a grey, weakly porous, ash-sized matrix. Clasts are typically 5–15 cm in diameter but, rarely, can be ~ 1 m across. Juvenile clasts dominate but small proportions of accidental clasts of Plinth Assemblage, granodiorite, monzonite and shale are present. Some juvenile clasts show vestiges of flow banding. The glassy clasts of rhyodacite display a weak, but obvious, subhorizontal fabric similar to eutaxitic fabrics observed in welded ignimbrites (*e.g.*, Smith, 1960a; Peterson, 1979). The welded facies is also characterized by pervasive coarse-scale (1–2 m), vertically-oriented, columnar jointing (Fig. 2a); the columns are continuous across the densely welded facies but are indistinct in the non-welded (basal) facies. The continuity of the columnar jointing suggests that, although the welded facies probably represents a multitude of individual depositional events, it constitutes a single cooling unit (Smith, 1960b; Wilson and Hildreth, 2003).

Observations of the incipiently welded facies derive from a ~ 5-m-thick volcaniclastic deposit that is weakly indurated, very poorly sorted and exposed at Field Site 2 (Table 1). The deposit is massive and unstructured except for a weak parallel alignment of the largest clasts; the long axes of these clasts are oriented parallel to the base. Clasts average 5–15 cm in diameter (rare exceptions can be ~ 1.5 m) and are supported by a matrix of oxidized, orange–brown ash (Fig. 2b). Juvenile clasts of rhyodacite are subangular to subrounded and, as a group, they vary greatly in vesicularity from pumice-like, to moderately vesicular, to less commonly dense and weakly vesicular ($\Phi \sim 5\%$). Some of the more vesicular and rounded juvenile clasts feature "breadcrust bomb" textures indicating a hot origin (Stewart et al., 2003); other juvenile clasts preserve flow banding developed prior to the fragmentation event. Rare accidental lithic clasts include Plinth Assemblage volcanic rocks and fine-grained monzonite.

Field Site 3 hosts the non-welded facies found at the top of the succession of block and ash flow deposits. Here, the deposit is ~ 5 m thick, poorly sorted, massive and unstructured. Most clasts are subangular to subrounded, lapilli and blocks of rhyodacite, and are supported in a matrix of grey–brown ash. Clasts average 5–15 cm in diameter although a few blocks are ~ 50 cm. Vesicularity of juvenile clasts ranges greatly, from nearly pumiceous to less abundant dense flow banded or glassy blocks. Accidental lithic clasts comprise 5–10% of the deposit and include the same lithologies as described above.

3. Petrography

The main petrographic features of the Pebble Creek Formation are described by Stasiuk et al. (1996), Hickson et al. (1999), and Stewart (2002). Here, ancillary petrographic (polarizing microscope and SEM) observations on samples from the block and ash flow deposits at Mount Meager are provided to assist in describing its componentry, the shape, and porosity of the pyroclasts, and the textural changes attributable to the welding process.

Deposits of the Pebble Creek Formation have a consistent mineralogy. The phenocryst assemblage is dominated by subhedral, complexly zoned, sieve-textured, plagioclase. Orthopyroxene, seen as euhedral, 0.2–0.4 mm crystals, is the dominant ferromagnesian phase. Amphibole occurs as subhedral crystals and as reaction rims on biotite crystals. Biotite occurs as highly corroded crystals or as cores to reaction rims of amphibole + oxides + pyroxene. Minor clinopyroxene and quartz are also present.

3.1. Non-welded facies

Juvenile pyroclasts from the non-welded to incipiently welded facies (Fig. 3) are vitric, variably vesicular, and can contain phenocrysts of plagioclase, orthopyroxene, amphibole, and biotite. Vesicles are commonly sub-spherical to elongate in shape, and range in size from 0.1–1.0 mm (Fig. 3a,b). Juvenile clasts are occasionally flow banded.

The matrix of the block and ash flow deposits is ash-rich and comprises juvenile vitric or vitrophyric clasts (Fig. 3c, d), abundant broken crystals (< 0.25 mm) (Figs. 3b, 4a), and minor accidental lithic clasts. The matrix is enriched in crystal fragments relative to the phenocryst contents of the juvenile vitrophyric clasts. The matrix porosity is relatively high and constitutes a network of connected pores between clasts. Some vitric clasts maintain substantial vesicularity (Fig. 3b, d, f), and some of these pores are likely to be isolated (Figs. 3d, 4f). The ash-sized matrix also contains phenocrysts jacketed by glass selvages; in some instances, the glass-jacketed phenocryst ensembles are fragmented (Figs. 3b, 4a). The finest ash particles (5–50 μm) commonly clump together or adhere to larger ash pyroclasts (Fig. 3e, f).

There are four main shard populations in the non-welded facies of the Keyhole Falls Member. Most shards (~ 60%) are blocky in habit (Fig. 3c, d); other shards have shapes dominated by bubble-walls (20%; Fig. 3c, d), are platy (10%; Fig. 3e), or are pumiceous (10%; Fig. 3f).

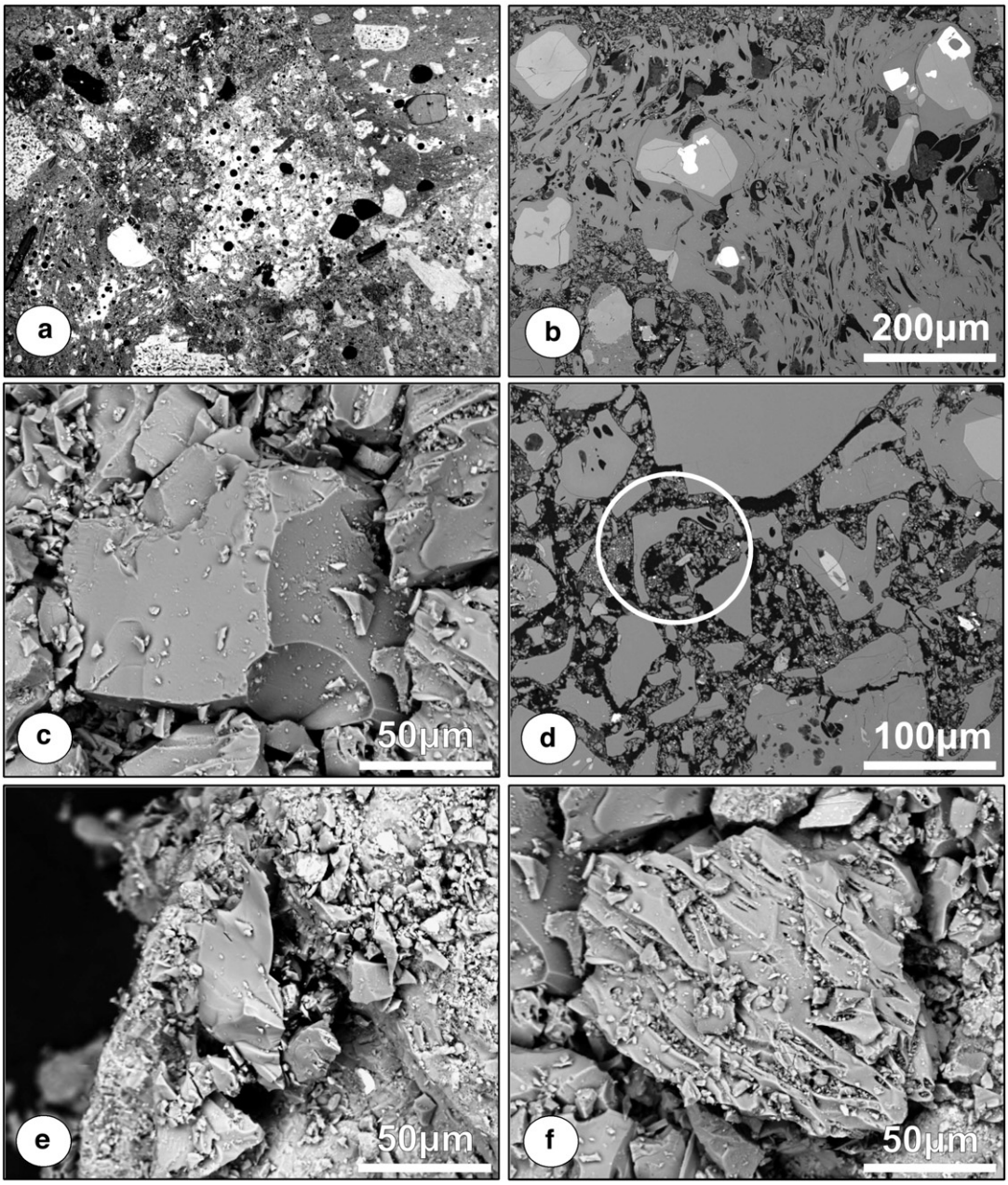

Fig. 3. Microscopic properties of clasts and shards in non-welded to incipiently welded block and ash flow deposits at Mount Meager. (a) Vesicular pumiceous clast (FOV=3.0 mm). (b) Pumiceous clast with stretched vesicles juxtaposed with dense shards of glass-jacketed crystals. (c–f) Images showing shapes and types of shards including, blocky, bubble-wall cuspate (circle, in d), platy, and pumiceous shards, respectively.

Larger pumiceous shards (500–1500 µm) contain abundant stretched or tubular vesicles (Fig. 3b). Otherwise, blocky, platy and bubble wall shards mainly feature spherical to elliptical vesicle shapes. Shard shapes are typically sharp, arcuate, curviinear, or angular, and show little evidence for mechanical abrasion during transport.

3.2. Welded facies

The mineralogy and componentry of the welded facies of the block and as flows are identical to that found in the non-welded facies. Shards from the welded facies remain somewhat angular, curvilinear, and arcuate in shape but are more elongate than those in

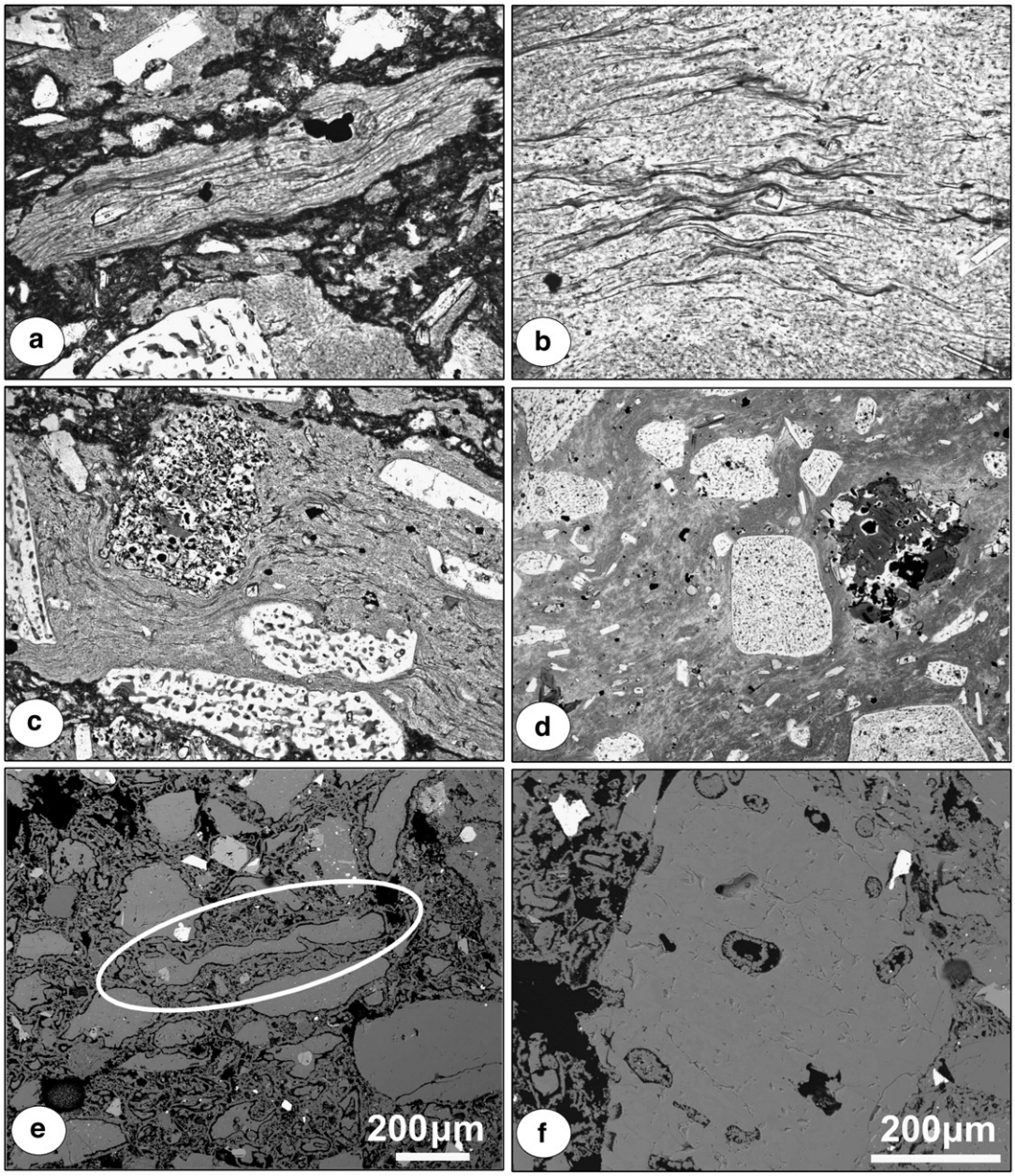

Fig. 4. Microscopic properties of clasts and shards in welded facies of the block and ash flow deposits at Mount Meager: (a) elongate clast showing collapsed vesicles (wispy structures) parallel to its length and parallel to macroscopic planar fabric in deposit (FOV = 3.9 mm); (b) close-up view of collapsed vesicles within a densely welded clast (FOV = 1 mm); (c–d) collapsed vesicles showing deformation of a clast around more rigid crystals (FOV = 3.9 mm); (e) elongate, flattened glass shard; (f) glass shard showing vapor-phase crystallization within isolated pores.

non-welded samples (Fig. 4a, e). The sense of elongation shared by all particles is parallel to the apparent fabric in the surrounding matrix, and is perpendicular to the flattening direction. The elongation and flattening of pyroclasts, at all scales, results in a planar alignment of particles that defines a foliation perpendicular to the direction of loading. At the outcrop scale, and in thin section, there is minor evidence for strain localization in the matrix around the margins of accidental fragments and crystals (Fig. 4c, d).

In outcrop and in hand sample, the block and ash flow deposits show an obvious densification with

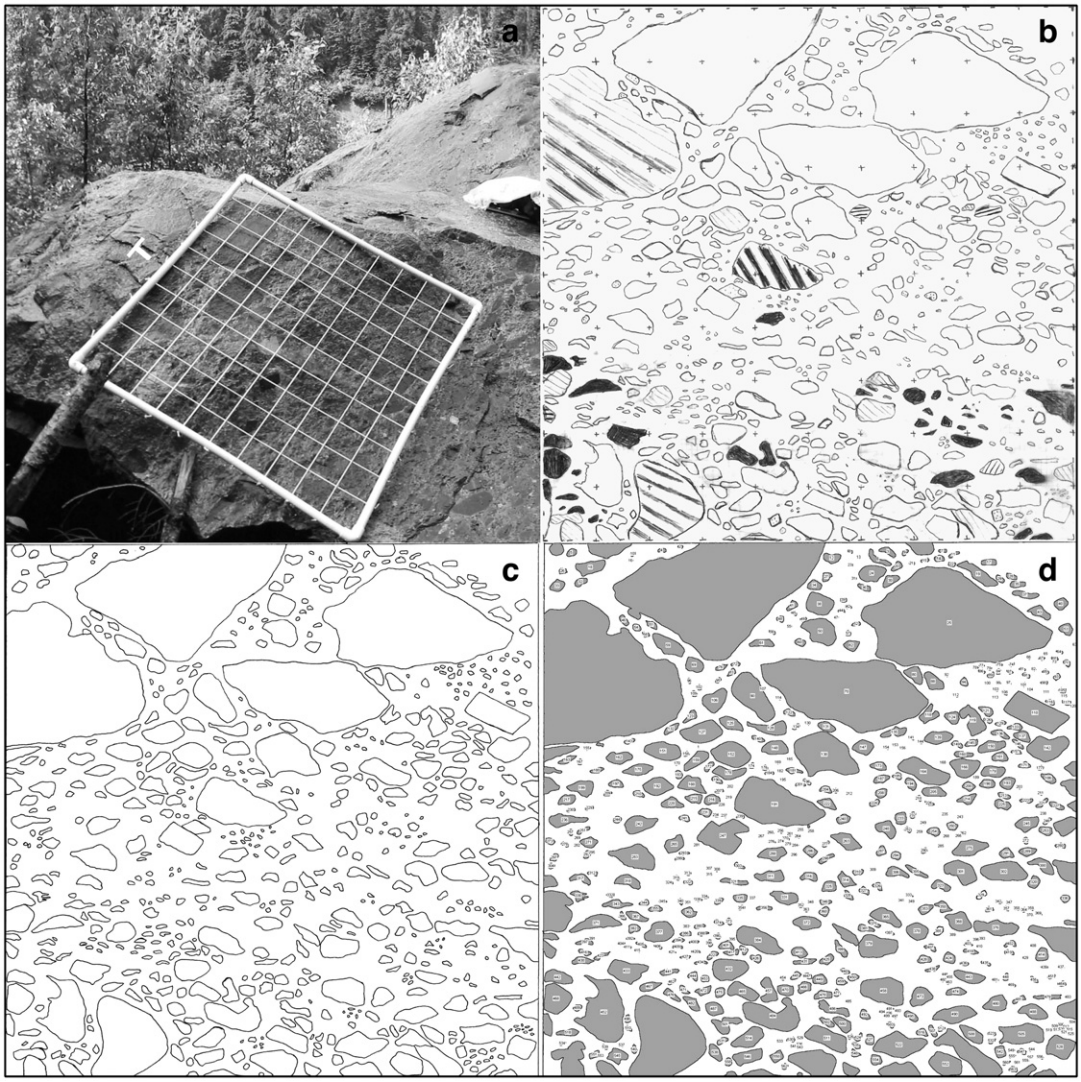

Fig. 5. Procedures for creating and analyzing field texture maps using FTM 01 as example: (a) field photo of 1 m × 1 m grid on outcrop of densely welded block and ash flow deposit (T denotes top of grid); (b) hand-drawn field texture map based on a minimum clast size of 0.5 cm; (c) digital scanned version used for image analysis (Scion Image™ or Image J™); (d) preliminary results of image analysis showing individual numbered clasts.

welding intensity. Based on textural features (Fig. 4), particle flattening and elongation are manifestations of deformation due to compactional strain accommodated by volume loss as evidenced by a reduction in porosity. Welding causes a substantial and visible reduction in porosity in both clasts (Fig. 4a, b, c) and matrix (Fig. 4d). In welded deposits, blocky, platy and bubble wall shards preserve few vesicles. Loss of porosity due to compaction is most evident in clasts that were originally vesicular and where collapsed pores have left behind wispy planar or linear structures (Fig. 4a, b). These wispy structures are also parallel to the length of the flattened clast. Evidence for compaction is less obvious in the most densely welded samples because they are fully annealed to produce a dense glassy matrix that obliterates this structure (Fig. 4d).

Some pitting and irregular surfaces are evident in larger shards, but primary vesicles are uncommon. As observed in the non-welded facies, fine ash particles (< 50 μm) stick to the larger shards and partially fill the pitted surfaces of the larger shards. In many densely welded samples, ~ 10% of shards larger than 500 μm preserve apparently undeformed vesicles that contain vapor-phase crystallization products (Fig. 4f).

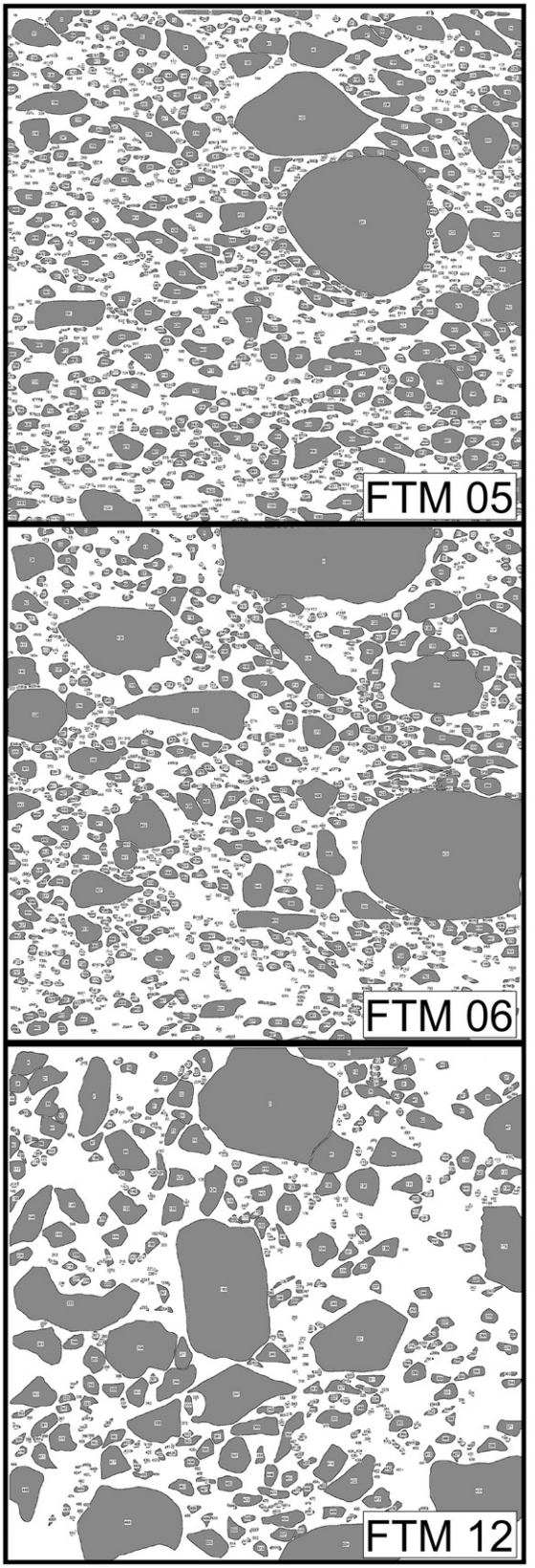

Fig. 6. Final digital images derived from three representative field texture maps. FTM 05 and 06 are from densely welded facies; FTM 12 is from incipiently welded deposit. See Fig. A1 (appendix) for 9 additional field texture maps.

4. Field texture maps

Fabric intensity has been used extensively to quantify strain in welded pyroclastic deposits (*e.g.*, Ragan and Sheridan, 1972; Sheridan and Ragan, 1976; Ui et al., 1989; Boudon et al., 1993; Karatson et al., 2002; Quane and Russell, 2006). We have used field texture maps (FTMs) of outcrops to describe and quantify compaction fabrics within the block and ash flow deposits. Image analysis of the texture maps, using software such as Scion Image™ and Image J™, provides metrics that characterize the nature of the pyroclastic deposits (*e.g.*, grain size distributions) and rank the amount of strain due to welding and compaction.

Field texture maps (FTMs) were made by placing a 1-m^2 grid against an outcrop (Fig. 5a) and hand-drawing each clast > 0.3 cm^2 onto the base map at a scale of 1:5 (Fig. 5b). The maps used a 10-cm^2 square grid for reference. All particles < 0.3 cm^2 (~ 0.5 cm in diameter) were treated as matrix. Twelve FTMs were drawn perpendicular to bedding and/or foliation and one map was oriented parallel to the plane of flattening (Fig. 6; Appendix Fig. A1). The FTMs were then retraced by hand (Fig. 5c), scanned, and imported into Scion Image™ and Image J™ for image analysis (Fig. 5d).

4.1. Image analysis results

Image analysis of the FTMs provides a variety of metrics that can be used to track welding intensity including the number of clasts, clast area, dimensions, orientation, and proportions (by area) of clasts and matrix. Clast-matrix proportions for FTMs are nearly constant, averaging 51 ± 5% (range = 43–59%; Fig. 7a), and are independent of welding intensity. Apparent grain size distributions (by area) derived from the FTMs show the poorly sorted nature of the block and ash flow deposits (Fig. 7b); distributions are slightly skewed away from smaller size fractions because the data sets are truncated below 0.3 cm^2. There is no variation in grain size distributions that can be related to welding intensity.

Clast oblateness is defined as $1 - c/a$, where c and a are the minimum and maximum clast diameters. This property increases with clast flattening and is used to track welding intensity (Quane and Russell, 2005a).

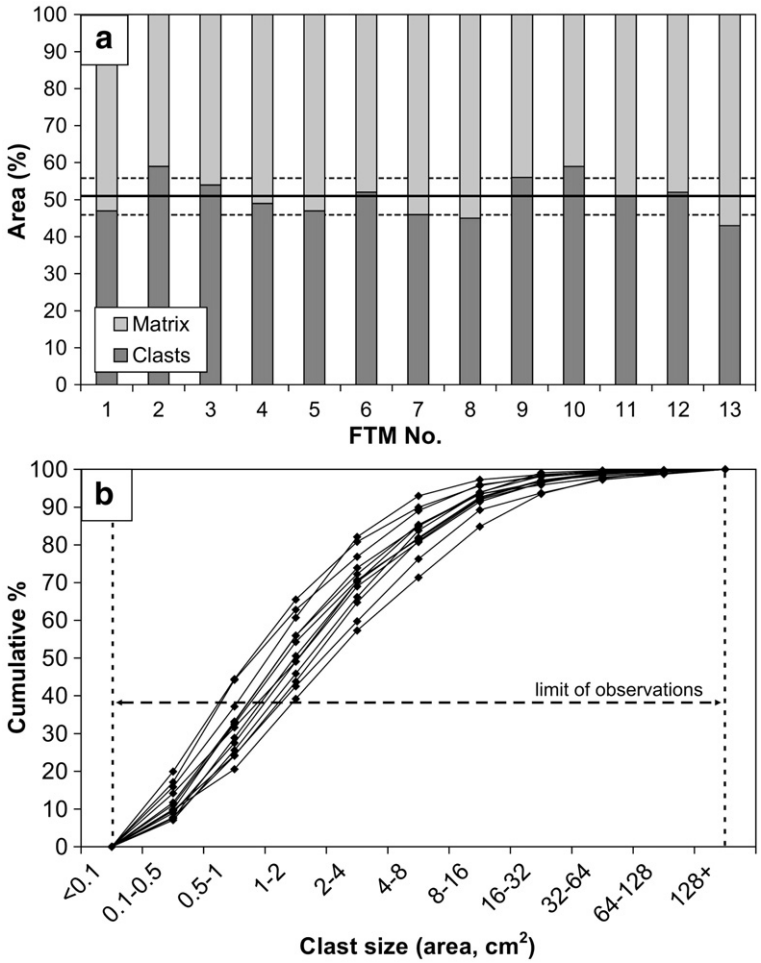

Fig. 7. (a) Proportions of clasts and matrix by area from analysis of FTM. Average proportion of clasts (< 0.3 cm^2) is 51%. Clasts never represent more than 60% of the total field texture map area. (b) FTM grain size distributions calculated on the basis of clast area using image analysis.

Clast orientation with respect to the horizontal (0°), has also been used as an indicator of welding intensity (Ragan and Sheridan, 1972; Sheridan and Ragan, 1976; Quane and Russell, 2005a). The average values of these two properties (Table 2) for each FTM are plotted in Fig. 8a; increased welding and compaction define a trend of decreasing clast orientation and increasing oblateness. The non-welded block and ash flow deposits show a relatively high average clast orientation (32–36°) and the lowest values of clast oblateness (0.32–0.35). FTMs for the densely welded block and ash flow deposits have lower average clast orientations (22–26°) and the highest values of clast oblateness (0.40–0.43).

The same textural mapping procedures were performed on multiple polished slabs (STMs) of these deposits (Fig. 8b) to explore the effects of welding at a reduced scale (75–200 cm^3). At the scale of these slabs, a single outcrop shows tremendous heterogeneity in these properties. For example, multiple slabs from Block 4 (Fig. 8b) show a range in average oblateness and clast orientation that nearly spans the full range found for the entire deposit. This is an indication that strain is much more localized at this scale.

Compactional strain due to volume loss (ε_V) for spherical particles relates to oblateness by:

$$\varepsilon_V = 1 - c/a. \quad (1)$$

Conversely, if strain conserves volume (*e.g.*, pure shear strain, ε_S), then:

$$\varepsilon_S = 1 - (c/a)^{2/3}. \quad (2)$$

Apparent values of ε_V and ε_S are reported in Table 2. Spherical clasts undergoing volume strain should show

Table 2
Summary of properties of block and ash flow deposits derived from image analysis of FTMs, including: total map area (A_T), number of particles (n), clast area (A), volume strain (ε_V), pure shear strain (ε_S), and % of clast (C) and matrix (M) by area

FTM	A_T (m^2)	n		A (cm^2)	Orientation (°)	ε_V*	ε_S**	C (%)	M (%)
1	1.00	563	avg.	5.68	23.61	0.42	0.31	47	53
			max.	440.49	–	0.85	0.71		
			min.	0.14	–	0.02	0.02		
2	0.98	386	avg.	12.14	26.16	0.40	0.30	59	41
			max.	2404.73	–	0.81	0.67		
			min.	0.23	–	0.04	0.02		
3	1.00	400	avg.	10.15	41.27	0.36	0.27	54	46
			max.	534.72	–	0.81	0.66		
			min.	0.22	–	0.02	0.01		
4	0.93	530	avg.	6.27	25.38	0.41	0.30	49	51
			max.	432.08	–	0.80	0.66		
			min.	0.22	–	0.01	0.01		
5	1.00	1064	avg.	4.19	21.74	0.41	0.31	47	53
			max.	592.70	–	0.83	0.69		
			min.	0.17	–	0.03	0.02		
6	1.00	883	avg.	3.57	24.97	0.43	0.32	52	48
			max.	189.97	–	0.92	0.82		
			min.	0.17	–	0.03	0.02		
7	0.88	487	avg.	5.95	34.07	0.32	0.23	46	54
			max.	166.89	–	0.80	0.66		
			min.	0.13	–	0.02	0.01		
8	0.93	571	avg.	6.24	31.31	0.32	0.23	45	55
			max.	194.92	–	0.80	0.66		
			min.	0.19	–	0.01	0.01		
9	0.79	613	avg.	4.22	26.68	0.38	0.28	56	44
			max.	148.97	–	0.79	0.65		
			min.	0.15	–	0.01	0.01		
10	0.60	340	avg.	5.52	29.28	0.37	0.27	59	41
			max.	337.07	–	0.79	0.64		
			min.	0.23	–	0.02	0.01		
11	1.00	370	avg.	10.26	35.94	0.33	0.24	51	49
			max.	332.90	–	0.79	0.65		
			min.	0.23	–	0.02	0.01		
12	0.91	505	avg.	7.28	28.35	0.39	0.29	52	48
			max.	396.44	–	0.87	0.75		
			min.	0.14	–	0.03	0.02		
13	0.76	436	avg.	6.83	31.62	0.35	0.26	43	57
			max.	212.23	–	0.71	0.57		
			min.	0.17	–	0.01	0.01		

*ε_V = volume strain from oblateness ($1-c/a$); **ε_S = pure shear strain estimated from oblateness ($1-c/a^{2/3}$).

a 1:1 relationship between oblateness and strain with a zero intercept (Fig. 8c inset). However, the high values of oblateness found in FTMs from non-welded deposits (0.32–0.35) suggest that clasts were deposited with an original oblateness of ~ 0.30. This is accounted for in Fig. 8c by the non-zero intercept, and would suggest < 15% compactional strain in samples of densely welded deposits having mean oblateness values in excess of 0.4.

This estimate of strain is anomalously low given the changes in texture, cohesion and porosity observed in outcrop and thin section. A digital experiment was designed to help interpret the relative amounts of strain in each FTM (Appendix Fig. A2). Beginning with the digital image of the FTM from the least welded deposit and assuming $\varepsilon_V=0$, we shortened the image in increments of 10%. The digital shortening experiment exactly simulates the strain due to compactional strain (volume loss). The resulting digital images serve as a '*Rosetta Stone*' for interpreting the relative strain represented by the other FTMs. Adopting this approach, the FTMs from the most densely welded block and ash

flow deposits (FTM 05, 06) most closely approximate the images corresponding to values of ε_V between 30% and 40% (Appendix Fig. A2). This experiment indicates that values of oblateness in this deposit qualitatively track relative strain but do not provide quantitative estimates of total strain.

5. Physical properties

Density and porosity are strongly coupled properties of pyroclastic rocks, and vary strongly with welding intensity (Smith, 1960a, 1960b; Ragan and Sheridan, 1972; Sheridan and Ragan, 1976; Quane and Russell, 2005a). We measured density and porosity on > 100 samples from all facies of the block and ash flow deposits. Bulk density (ρ_B) is the density of the rock including all of its pore space (*e.g.*, connected and isolated porosity) and derives from measurements of mass and volume on consolidated (cores) and unconsolidated (graduated cylinder) materials. Skeletal density (ρ_S) is the density of the rock and its isolated (non-penetrated) porosity and is measured by helium pycnometry. The density of finely crushed rock powders (ρ_R) was also measured by helium pycnometry and is the density of the solid material alone.

These values of density allow for computation of three forms of porosity (Φ), total (T), connected (C) and isolated (I):

$$\Phi_T = 1 - \frac{\rho_B}{\rho_R} \quad (3)$$

$$\Phi_C = 1 - \frac{\rho_B}{\rho_S} \quad (4)$$

$$\Phi_I = \frac{\rho_B}{\rho_S} - \frac{\rho_B}{\rho_R}. \quad (5)$$

A summary of physical property measurements is given in Tables 3–5 and the complete dataset can be found as Online Resources Tables A1 and A2.

5.1. The 'proto-deposit'

The initial properties of the block and ash flow deposits, prior to welding and compaction, are based on measurements of the unconsolidated portions of the block and ash flow deposits (Table 3). Minimum estimates of bulk density for seven samples from the non-welded to incipiently welded facies were obtained by measuring mass and volume of loose sample that was tightly packed into a graduated cylinder (not *in situ*). Values range from 1.39–1.59±0.06 g/cm^3. Skeletal density, based on helium pycnometry, shows less variation: 2.50–2.54±0.003 g/cm^3. Lastly, the density measurements of powdered matrix samples show little variation (2.53–2.55±0.01 g/cm^3) and are only slightly higher than values for ρ_S. The measured values of density imply a range in total porosity for the non-welded and unconsolidated matrix of 38–45%, where 37–45% is connected, and 0.19–0.95% is isolated.

Large clasts of rhyodacite from the unconsolidated deposits have bulk density values ranging from 1.50–1.89±0.02 g/cm^3. Values of ρ_S show less variation: 2.24–2.52±0.01 g/cm^3 and rock powder densities have values of 2.46–2.59±0.01 g/cm^3. These values imply a total porosity for clasts of lava varying between 24% and 40%; connected porosity spans 19–34% and isolated porosity is estimated at 0–12%.

5.2. Bulk density

The range in bulk density for samples of clasts, matrix, and mixtures of both is substantial (1.45–2.40 g/cm^3), and can be ascribed to variations in total porosity (Tables 4, 5; Fig. 9; Online Resources Table A1). Matrix samples have a narrower range and higher values of bulk density than do clasts (Fig. 9a). Both clasts and matrix show an increase in bulk density as welding intensifies (Table 5). Average clast density increases from 1.68±0.12 g/cm^3 (non-welded) to 2.01±0.06 g/cm^3 in the incipiently welded facies, and to 2.34±0.04 g/cm^3 when welded. Bulk density of the matrix increases with welding from a mean value of 1.46±0.05 g/cm^3 for incipiently welded facies to 2.13±0.08 g/cm^3 for densely welded facies. Samples comprising a mixture of matrix and clasts from the welded facies have intermediate values (2.26±0.08 g/cm^3).

5.3. Skeletal density

The variations in ρ_S result from the presence of isolated porosity and/or differences in rock powder density. For this sample suite, values of ρ_S are substantially higher than the corresponding values of ρ_B (Fig. 9b), and the total range in ρ_S (Fig. 9b) is small (2.2–2.6 g/cm^3) relative to variations in ρ_B. Matrix samples tend to have higher values of ρ_S, although the differences between clast and matrix are slight.

Samples from non-welded to incipiently welded facies have skeletal densities of 2.31–2.46 g/cm^3 compared to ρ_S values of 2.51–2.52 g/cm^3 for moderately to densely welded facies. Juvenile clasts show a small increase in skeletal density as welding intensifies (2.37±0.09 g/cm^3 to 2.46±0.02 g/cm^3),

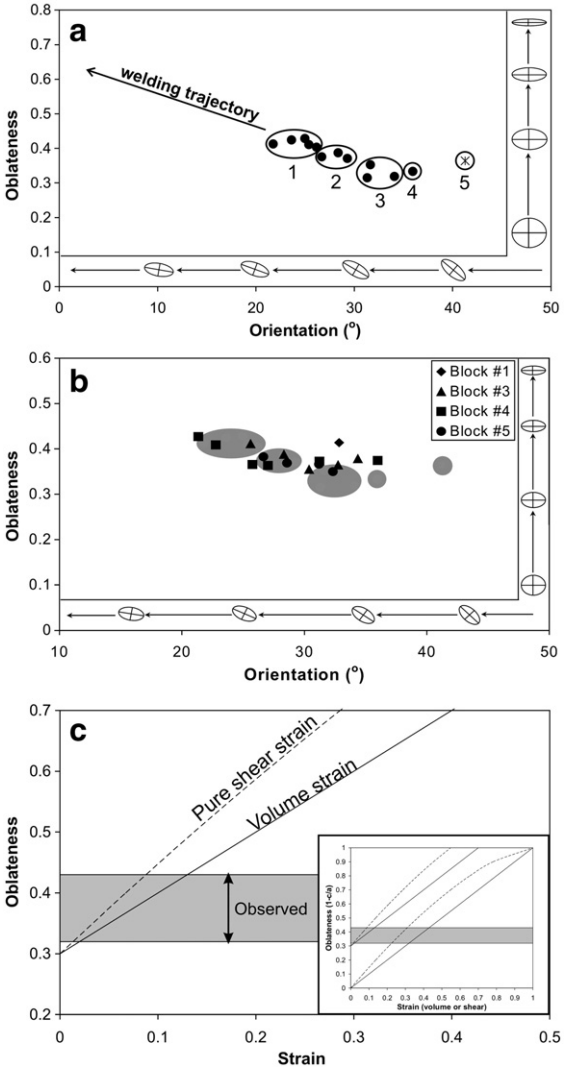

Fig. 8. Results from analysis of field texture maps. (a) Average clast orientation plotted against average clast oblateness for FTMs after grouping by facies: (1) densely welded, (2) upper, incipiently welded, (3) basal, non-welded, (4) upper, non-welded and, (5) densely welded facies mapped on the foliation surface. (b) STMs from the densely welded facies (Blocks 1–5) overlap the entire range defined by FTMs (a). (c) Analysis of strain based on oblateness $(1-c/a)$ and assuming either pure compactional strain (solid line) or pure shear strain (dashed line). Shaded field denotes range of oblateness found in the block and ash flow deposits (see text).

however variations in ρ_S for matrix samples are within analytical uncertainty.

5.4. Rock powder density

The range of ρ_R is extremely narrow (Fig. 9c), indicating that there is little difference in the properties of dense rock equivalent samples, and that most of the variation in ρ_S (Fig. 9b) can be attributed to the presence of isolated porosity (see Fig. 10a). Values of ρ_R for all samples vary from 2.48 to 2.53±0.04 g/cm^3 independent of welding intensity. Values of ρ_R for clasts (2.48 to 2.50±0.03 g/cm^3) are slightly less than for matrix samples (2.54 to 2.55±0.03 g/cm^3.

5.5. Analysis of porosity

Total porosity for all samples, including both connected and isolated porosity, ranges from near 0 to 45% (Table 5; Fig. 10). Clasts from non-welded deposits have an average Φ_T of 32.4±4.8% which decreases to 18.9±2.3% in the incipiently welded facies, and to 5.35±1.1% in the densely welded facies. The average Φ_T for matrix samples is 40.3±3.0% in non-welded deposits and is reduced to 16.6±3.0% in the densely welded facies. Connected porosity is computed from skeletal density measurements (Tables 4, 5; Fig. 10a). Clasts from non-welded facies have an average Φ_C of 29.0±3.8% which decreases to 16.0±1.6% when incipiently welded, and to 4.79±1.0% when densely welded. On average, Φ_C for matrix samples is 39.9±3.0%, which is reduced by welding to 16.3±3.0%.

A comparison of total to connected porosity (Fig. 10a; Eqs. (3)–(5)) demonstrates the magnitude and distribution of Φ_I in these samples. All samples plotting below the 1:1 line in Fig. 10a have measurable Φ_I. Isolated porosity varies between 0 and 8% and is highest in the samples having the highest Φ_T. Values of Φ_I for matrix samples are generally less than 1% (Table 5)). The highest average isolated porosity occurs in juvenile clasts from the non-welded facies (3.45±2.2%), but is reduced to near zero (0.94±1.0%) in the densely welded deposits. In general, isolated porosity decreases with welding and, where $\Phi_T < 20\%$, Φ_I is absent. During the welding process, both connected and isolated porosity are drastically reduced: for example, Φ_C is reduced to 5% and Φ_I is reduced to ≤ 1% in the dense, vitrophyric clasts. Values of measured isolated porosity that are less than zero are within error of zero and result from combined measurement uncertainties in ρ_B, ρ_S and ρ_R (see Eq. (5)).

6. Discussion

Welding is characterized by the coalescence of hot glassy pyroclasts (sintering) and typically involves concomitant flattening or stretching of pyroclasts due to a compactional load (Smith, 1960b; Guest and Rogers, 1967; Riehle et al., 1995). Generally, welding processes require temperatures above the melt's

Table 3
Summary of physical properties of bulk samples of unconsolidated block and ash flow deposits, including: bulk density (ρ_B), skeletal density (ρ_S), rock density (ρ_R), total porosity (Φ_C), and isolated porosity (Φ_I). Analytical uncertainties are reported as 1σ

Sample	ρ_B (g/cm^3)	σ	ρ_S (g/cm^3)	σ	ρ_R (g/cm^3)	σ	Φ_T (%)	σ	Φ_C (%)	σ	Φ_I (%)	σ
KM-04-018 [a]	1.47	0.003	2.50	0.003	2.54	0.006	42.11	0.17	41.15	0.13	0.95	0.25
KM-04-019 [a]	1.48	0.012	2.52	0.002	2.55	0.002	42.07	0.48	41.25	0.49	0.82	0.12
KM-04-020 [a]	1.52	0.014	2.52	0.002	2.53	0.002	39.76	0.57	39.51	0.57	0.25	0.10
KM-04-031 [b]	1.59	0.025	2.54	0.002	2.55	0.002	37.77	0.98	37.35	0.98	0.42	0.10
KM-05-023 [c]	1.54	0.028	2.52	0.003	2.55	0.003	39.53	1.11	38.73	1.13	0.80	0.14
KM-05-032 [a]	1.39	0.028	2.52	0.001	2.53	0.004	45.03	1.09	44.84	1.09	0.19	0.15
KM-05-036 [b]	1.43	0.057	2.53	0.001	2.54	0.001	43.55	2.26	43.49	2.27	0.06	0.07

[a] Upper incipiently welded deposits.
[b] Basal non-welded deposits.
[c] Upper non-welded deposits.

characteristic glass transition temperature (Giordano et al., 2000; Giordano et al., 2005; Russell and Quane, 2005). Factors that govern welding intensity include melt rheology, emplacement temperature, volatile content, mass flux during deposition, cooling history, deposit thickness, permeability, and particle size distributions (Sparks et al., 1999; Giordano et al., 2000; Quane and Russell, 2005b; Russell and Quane, 2005). Above, the composition and physical properties of a unique sequence of welded block and ash flow deposits have been described. Below, the origins of these welded deposits are explored in more detail.

6.1. The welding and compaction process

Density and porosity correlate strongly with welding intensity and we use the reduction in porosity to calculate the total strain (ε_T) due to compaction (volume strain):

$$\varepsilon_T = \frac{\Phi_o - \Phi_f}{1 - \Phi_f} \quad (6)$$

where Φ_o and Φ_f are the original and final porosity (Quane and Russell, 2006). If these welded pyroclastic deposits also underwent appreciable shear strain (constant volume) then our values of ε_T are minima. Most evidence suggests that porosity reduction is sufficient to explain the extent of welding. For example, particle oblateness is low relative to the amount of strain implied by porosity reduction. Pure shear strain appears only to have played a role locally where strain is intensified around solid particles. Eq. (6) requires estimates of the original (pre-welding) porosity of the block and ash flow deposits; these properties derive from measurements on the unconsolidated facies of the block and ash flow deposits. The maximum porosities measured for clast and matrix are 40% and 45%, respectively (Online Resource Tables A1 and A2). The calculated strain–porosity relationships for clasts and matrix (Eq. (6)) are parallel and separated only by the differences in starting porosity (Fig. 10b). Moreover, clasts and matrix define the same degree of maximum strain (~ 38%) suggesting that the deformation of clasts and matrix is fully coupled.

Isolated porosity is mainly present in the non-welded or low-strain clasts (Fig. 10b; inset). Perhaps unexpectedly, welding and compaction destroys both Φ_C and Φ_I rather than producing additional Φ_I by cutting off connections between pores (Fig. 10a). The fact that new

Table 4
Summary of density (g/cm^3) and porosity (%) data listed by welding facies of the block and ash flow deposit. Analytical uncertainties are reported as 1σ

Facies	n	ρ_B		ρ_S		ρ_R		Φ_T		Φ_C		Φ_I	
		Avg.	σ	Avg.	σ	Avg.	σ	Avg.	σ	Avg.	σ	Avg.	σ
Upper non-welded	16	1.70	0.122	2.46	0.061	2.52	0.032	32.65	4.88	31.01	4.76	1.65	1.357
Incipiently welded	12	1.83	0.275	2.44	0.062	2.50	0.029	27.40	11.96	25.35	13.07	2.04	1.596
Densely welded	57	2.19	0.113	2.51	0.040	2.52	0.034	13.49	5.41	13.08	5.51	0.48	1.070
Moderately welded	6	2.08	0.041	2.52	0.030	2.53	0.012	17.55	1.59	17.23	2.16	0.32	1.029
Basal non-welded	15	1.64	0.126	2.31	0.069	2.49	0.023	33.89	5.64	28.92	5.30	4.97	1.696
All samples	**106**	**1.99**	**0.273**	**2.47**	**0.084**	**2.52**	**0.033**	**21.21**	**10.88**	**19.81**	**10.05**	**1.44**	**1.966**

Table 5
Summary of density (g/cm^3) and porosity (%) data for samples of clasts and matrix from block and ash flow deposits. Analytical uncertainties are reported as 1σ

Component	Facies	n	ρ_B		ρ_S		ρ_R		Φ_T		Φ_C		Φ_I	
			Avg.	σ	Avg.	σ	Avg.	σ	Avg.	σ	Avg.	σ	Avg.	σ
Clasts	Non-welded	28	1.68	0.12	2.37	0.09	2.50	0.03	32.39	4.75	28.95	3.83	3.45	2.16
	Incipiently welded	8	2.01	0.06	2.41	0.04	2.49	0.02	18.91	2.25	16.01	1.58	2.90	1.36
	Welded	11	2.34	0.03	2.46	0.02	2.48	0.03	5.35	1.07	4.79	0.99	0.94	1.02
Matrix	Non-welded	3	1.52	0.08	2.53	0.01	2.55	0.01	40.28	2.96	39.86	3.22	0.43	0.37
	Incipiently welded	4	1.46	0.05	2.51	0.01	2.54	0.01	42.24	2.16	41.69	2.25	0.55	0.39
	Welded	46	2.13	0.08	2.52	0.03	2.54	0.02	16.63	2.95	16.29	3.03	0.33	1.05
Mixed	Welded	6	2.26	0.08	2.49	0.05	2.50	0.03	9.63	3.33	9.10	3.52	0.56	1.10
All samples		**106**	**1.99**	**0.27**	**2.47**	**0.08**	**2.52**	**0.03**	**21.21**	**10.88**	**19.81**	**10.05**	**1.44**	**1.97**

Φ_I is not created during welding, implies that gas escape processes are operating on faster timescales than are the rates of viscous flow. However, the destruction of isolated (fluid-filled) porosity requires further examination. During compaction, it is possible that isolated fluid-filled pores serve to localize strain and deform to higher degrees becoming extremely flattened and ultimately non-detectable. Alternatively, the volatiles trapped in isolated pores may, in response to lithostatic load, be resorbed by the surrounding melt or glass (Sparks et al., 1999). The resorption of volatiles allows a simultaneous reduction in melt viscosity and fluid pressure in the isolated pores thereby facilitating viscous collapse of vesicles.

Fig. 11 summarizes a series of scenarios for partitioning of strain between clasts and matrix in welded pyroclastic deposits. Ash flow tuffs and clastogenic lavas represent end-members where the componentry of the deposit dictates that all strain is accommodated by the matrix or by the clasts, respectively. The upper half of the diagram displays deposits, such as many ignimbrites, where pumiceous clasts deform earlier and more intensely than the surrounding matrix (Fig 11; Ragan and Sheridan, 1972). The pumices deform more easily because of their lower effective viscosity due to higher porosity and, perhaps, higher water contents (*e.g.*, Ross and Smith, 1961; Ragan and Sheridan, 1972). The pumices continue to collapse until they form fiamme and achieve a higher viscosity (strain hardening) than the enclosing ash-rich matrix; subsequent strain is preferentially absorbed by the matrix rather than by the fiamme. The lower half of the diagram is for deposits where the matrix deforms more efficiently than the clasts; welded lithic breccias may serve as an example of this path. Values of strain for corresponding pairs of matrix and clast from the block and ash flow deposits are plotted on Fig. 11. These data plot on the 1:1 line indicating that compactional strain due to welding was accommodated equally by the rhyodacite clasts and the host matrix.

6.2. Original deposit thickness

The maximum strain for the deposit is 38% and suggests that the wedge-shaped deposit of welded block and ash flows (Fig. 12) has undergone considerable shortening due to compaction. The deposit is thickest at Keyhole Falls (Fig. 2a) and currently comprises a single ~ 112-m cooling unit of welded block and ash flow deposits overlain by another ~ 60–75 m of intercalated alluvial, non-welded pyroclastic, and rock avalanche deposits. Average estimates of strain are used for each welded facies of the block and ash flow deposits to compute the average strain for the 112-m-thick cooling unit exposed at Keyhole Falls (Fig. 12a) from:

$$E_{Avg} = \sum_{i=1}^{n} (h_i \cdot \varepsilon_i)/H \quad (7)$$

where h_i is the thickness of each of the n facies-intervals, ε_i is the average strain for that section, and H is the total thickness of the section (Quane and Russell, 2005a). The integrated strain is estimated at ~ 31% for the block and ash flow deposits which is 12–15% lower than values computed for other notable welded pyroclastic deposits: (1) 43% for the Bishop Tuff, California; (2) 46% for the Bachelor Mountain Tuff; and (3) 45% for Therasia welded air-fall tuff (*cf.* Quane and Russell, 2005a).

We have used this estimate of integrated strain (31%) to restore the stratigraphic section exposed at Keyhole Falls (Fig. 12a) to its original thickness. Our calculations suggest that the 112-m-thick section resulted from 50 m of shortening of the original thickness of ~ 162 m. Strain estimates were also used to create a 3D representation of the welded block and ash flow deposits filling the

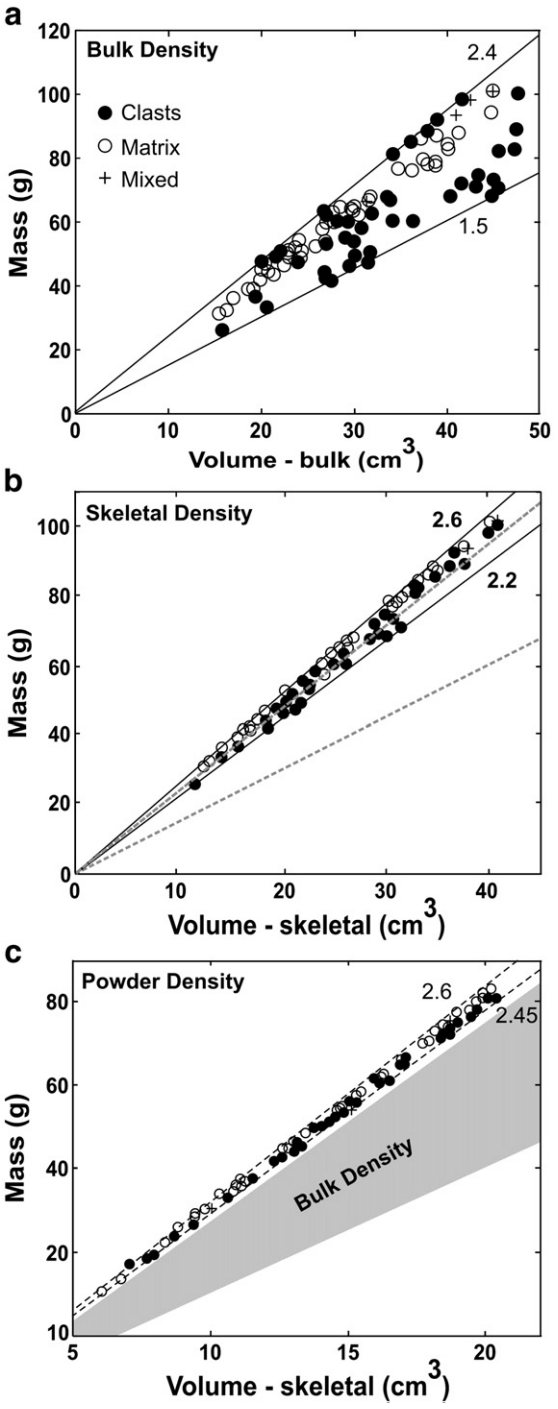

Fig. 9. Mass–volume plots for all samples (see Tables A1 and A2) define total ranges of (a) bulk density (ρ_B), (b) skeletal density (ρ_S), and (c) rock powder density (ρ_R) for samples of clasts, matrix, and mixed samples. Minimum and maximum densities are denoted by solid or dashed lines and labeling. Shading in (c) represents range in bulk density shown in (a).

Lillooet River valley (Fig. 12b), which depicts the greatest vertical shortening at Keyhole Falls, and progressively less (absolute) shortening downstream.

6.3. Implications of porosity distributions

Physical properties of the Mount Meager block and ash flow deposit sample suite provide a basis for comparing this non-welded to welded block and ash flow deposit to other volcanic deposits. Below we compare porosity data for samples of the block and ash flow deposit at Mount Meager to porosity data of: (1) pumices from Plinian to Vulcanian explosive eruptions (Mount Meager, Rust et al., 1999; Lascar Volcano and Soufrière Hills, Formenti and Druitt, 2003); (2) breadcrust bombs from Guagua Pichincha (Wright et al., 2007); (3) rhyodacite, andesite, and basalt lavas (Rust et al., 1999); and (4) lava blocks

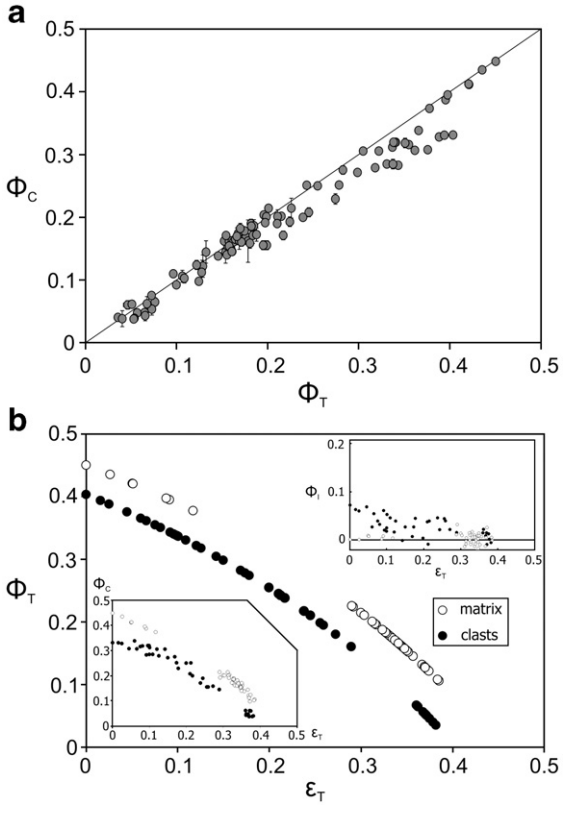

Fig. 10. Measured values of fractional porosity and values of strain calculated from porosity. (a) Total porosity (Φ_T) *vs.* connected porosity (Φ_C). Samples lying below the 1:1 line (solid line) contain isolated porosity represented by the vertical distance to the 1:1 line. (b) Total volume strain (ε_T) is calculated assuming initial porosity for clasts (40%) and matrix (45%) and plotted against observed Φ_T; insets show the reduction of isolated (Φ_I) and connected (Φ_C) porosity with strain in clasts and matrix.

from dome-collapse pyroclastic flow deposits at Soufrière Hills, Merapi, Cayambe, and Mount St. Helens (*cf.* Formenti and Druitt, 2003).

This comparison is facilitated by plotting total porosity (Φ_T) *vs.* connected porosity (Φ_C) (Fig. 13). The presence and magnitude of isolated porosity (Φ_I) are identified by points that plot below the 1:1 line. We begin by plotting data from the literature for samples from deposits resulting from explosive volcanic events (Fig. 13a). The sample suites include: pumices from pumiceous pyroclastic flow deposits from Mount Meager (Rust et al., 1999), pumice blocks from fountain collapse events associated with Vulcanian eruptions at Lascar Volcano and Soufrière Hills (Formenti and Druitt, 2003), and breadcrust bombs from Guagua Pichincha (Wright et al., 2007). Pumices from Mount Meager, Lascar Volcano, and Soufrière Hills have Φ_T values of 52–75% and a maximum of 11% isolated porosity (Fig. 13a). Breadcrust bombs from Guagua Pichincha have total porosities of 32–71% (except for one sample), and can have up to 12% isolated porosity. All of these products of explosive volcanism show the presence of substantial Φ_I except at values of $\Phi_T < 40\%$ (Fig. 13a). In contrast, values of porosity measured on samples of lavas and lava blocks from dome-collapse pyroclastic flows (Fig. 13b) tend to have little or no Φ_I despite the broad range in total porosities (2–59%). The only exceptions are samples of the Mount St. Helens cryptodome in the blast deposit that contain up to 5% isolated porosity at total porosities of ~ 50%.

Our data on the welded block and ash flow deposits (Fig. 13c, d) show the matrix samples to have minimal isolated porosity (< 3%) regardless of welding intensity. However, clasts of rhyodacite lava in these deposits have up to 40% porosity of which up to 8% is isolated. The maximum value of Φ_I is found in the non-welded to incipiently welded facies, where clasts contain 20–40% total porosity (Online Resources Table A2). Whereas samples from lavas and lava-dome-collapse-events (Fig. 13b) lack isolated porosity even at high values of Φ_T, the juvenile clasts from the non-welded block and ash flow deposits at Mount Meager contain measurable Φ_I. Furthermore, rhyodacite clasts within the block and ash flow deposits at Mount Meager show similar values (< 8%) of Φ_I as pumices and breadcrust bombs (Fig. 13a). In fact, our samples maintain an isolated porosity to lower (~ 20%) values of Φ_T.

Formenti and Druitt (2003) explain the presence of Φ_I as a second bubble nucleation event associated with eruption. Their examination of samples under SEM identified two populations of bubbles in the pumice samples: (i) a set of large, connected vesicles, and (ii) a group of smaller, isolated vesicles. The key to producing isolated porosity appears to be the capacity for the magma to undergo two bubble nucleation events prior to eruption. The first population nucleates, grows and coalesces as magma ascends in the conduit. The second population forms during the penultimate depressurization event immediately prior to eruption. At this point, the magma is still above its glass transition temperature and the rapid pressure reduction attending the explosive eruption allows for the production of a second generation of vesicles. These vesicles are smaller, isolated, and will remain isolated if they are efficiently quenched (thereby preventing growth and coalescence) during eruption and transport.

On this basis, explosive eruptions (*e.g.*, column-collapse pyroclastic density currents, cryptodome blasts, Vulcanian explosions) favour the production and preservation of isolated porosity, whereas isolated porosity, if produced, is rarely preserved by effusive events (Formenti and Druitt, 2003). In the data sets shown in Fig. 13, all pumice samples from column-collapse pyroclastic density currents, breadcrust bombs (Fig. 13a), and samples of Mount St. Helens cryptodome blast deposits (Fig. 13b) possess isolated porosity. Samples of lavas and blocks from lava-dome-collapse feature only connected porosity. The extrusion of lava and lava domes is fed by magma that possesses a population of bubbles that nucleated, grew, and coalesced continuously during rise in the conduit. Without a second pronounced depressurization event, there is no catalyst to produce a distinct population of isolated bubbles. Furthermore, slower quench rates may also act against preserving isolated porosity in lavas and lava-domes.

In the case of pyroclastic density currents produced by the gravitational collapse of domes, there is also no opportunity to produce a population of isolated vesicles. Once erupted, domes will cool to below their glass transition temperatures and therefore, even if the gravitational collapse causes a substantial depressurization event, the glass cannot produce the requisite second population of (isolated) vesicles. A notable exception would be the case where collapse events cored deeply into a large dome that grew endogenously; such an event would supply the requisite depressurization event and expose material that could still be above its glass transition temperature. The result would be the production of isolated porosity that would be quenched during emplacement of the pyroclastic density current. The Mount St. Helens cryptodome may represent another special situation in which magma is intruded close to the surface but is maintained above its glass transition until the point of eruption. The landslide-induced depressurization event caused its exposure and eruption and became a catalyst for a second nucleation event producing

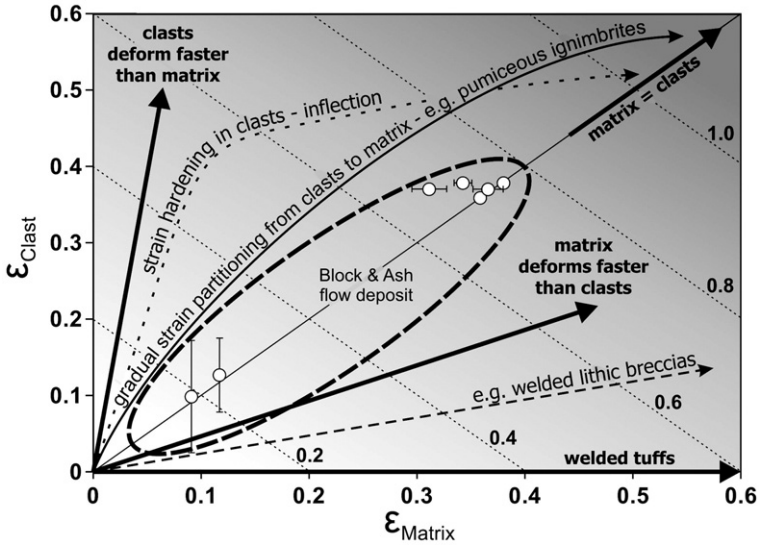

Fig. 11. Conceptual diagram showing possible paths controlled by partitioning of strain between matrix and clasts. Samples of welded block and ash flow deposit record equal strain (1:1) in clasts and matrix.

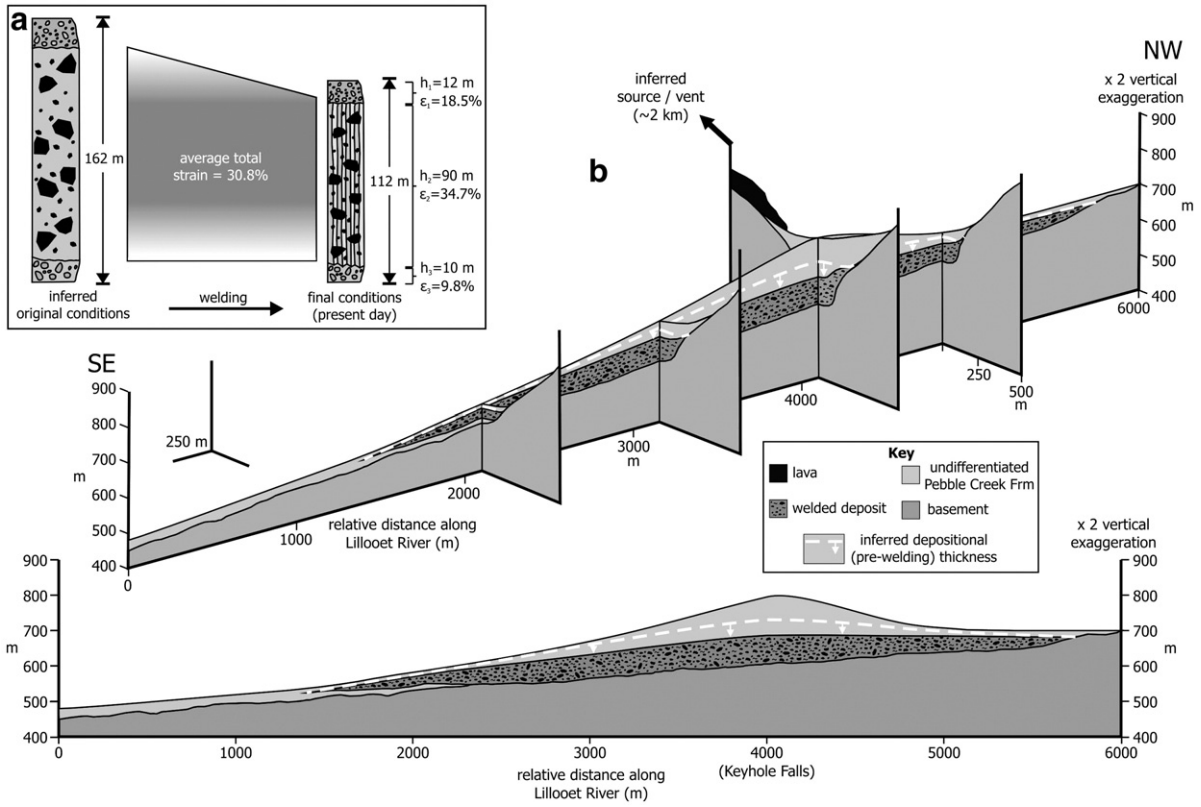

Fig. 12. Schematic representation of the original pre-welding distribution of block and ash flow deposits. (a) A single 112 m thick cooling unit exposed at Keyhole Falls (Fig. 2a) represents an original thickness of > 160 m (assuming an integrated strain of 31%). (b) A 3-D representation and longitudinal cross-section of the deposit shown with the current and original (white dashed line) pre-welding geometry.

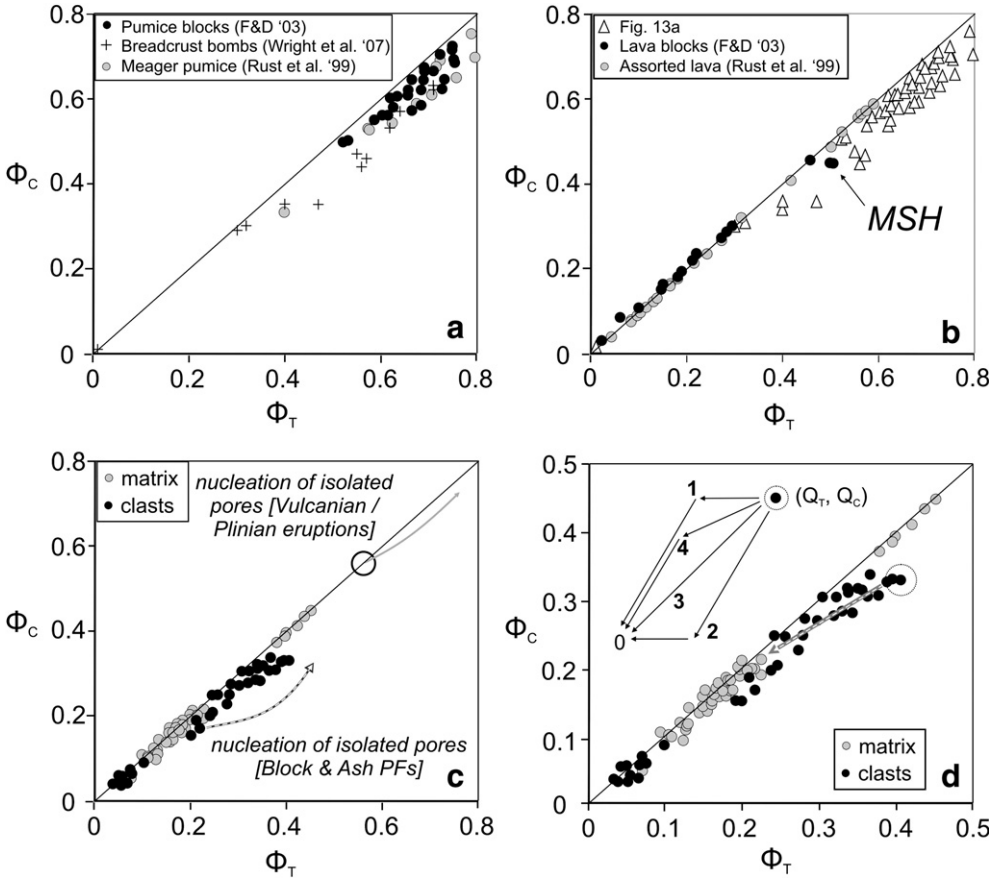

Fig. 13. Plots of total porosity (Φ_T) *vs.* connected porosity (Φ_C) for: (a) pumices from Mount Meager (Rust et al., 1999), pumiceous blocks Lascar Volcano, and Soufriere Hills (Formenti and Druitt, 2003), and breadcrust bombs from Guagua Pichincha (Wright et al., 2007), (b) data from (a) *vs.* data for lava blocks from Soufriere Hills, Merapi, Cayambe, Mount St. Helens (Formenti and Druitt, 2003) and samples of assorted lavas (Rust et al., 1999), (c) conceptual paths that produce isolated porosity during decompression associated with explosive eruption are shown for Vulcanian to Plinian eruptions and for explosive volcanism producing block and ash flow deposits at Mount Meager. (d) Same data as in (c); inset summarizes possible paths for porosity reduction during welding and compaction: (1) loss of Φ_I until consumed, followed by loss of Φ_C, (2) loss of Φ_C followed by reduction of Φ_I, (3) both Φ_C and Φ_I are lost simultaneously and in proportion to their original abundances, and (4) Φ_C and Φ_I are lost equally (independent of proportions) until all isolated porosity is removed. Data from this study are most consistent with path (4) (see circle and arrow).

small isolated vesicles as measured by Formenti and Druitt (2003) (Fig. 13b).

The non-welded to incipiently welded clasts of rhyodacite in the block and ash flow deposits retain significant isolated porosity (Fig. 13c, d). The presence of isolated porosity in all juvenile clasts (except those from the densely welded facies) suggests the possibility of an explosive origin: a major depressurization event causing fragmentation of the magma while above its glass transition temperature and producing a late population of isolated vesicles. The consequence is that these pyroclastic flows are unlikely to have been produced by simple gravitational collapse of lava domes (*e.g.*, Merapi-type; Bardintzeff, 1984; Sato et al., 1992; Boudon et al., 1993; Ui et al., 1999; Miyabuchi, 1999; Abdurachman et al., 2000). A much more likely analogue is represented by the eruption of Soufrière Hills, Montserrat, where the explosive collapse of hot, young lava domes was triggered by Vulcanian eruption (*e.g.*, Cole et al., 2002; Woods et al., 2002; Formenti and Druitt, 2003).

There are several ancillary lines of evidence suggesting a hot explosive origin (Soufrière-type) for these deposits. Breadcrust bombs can be found in the non-welded facies at the top and bottom of the succession and are indicative of a hot, explosive pyroclastic origin (*e.g.*, Miyabuchi, 1999; Wright et al., 2007). In addition, the sequence of block and ash flow deposits forms a single wedge-shaped (112–25 m thick; Fig. 12) cooling unit that has a densely welded interior. The densely welded facies also features metre-scale, vertical columnar jointing indicating a single cooling unit. These observations imply that the block and ash flow events had to be

emplaced at high temperatures in excess of its glass transition temperature in order to sustain this degree of welding (*e.g.*, Giordano et al., 2005; Russell and Quane, 2005) and that the entire package was emplaced rapidly. Arguing against a purely explosive origin, is the fact that there are few fallout deposits and no blast deposits identified that can be ascribed to an eruption-induced explosive collapse of hot domes. This lack of stratigraphic record may result from the lack of preservation of fall deposits on the steep slopes of the Lillooet River valley, and subsequent mixing of Vulcanian tephra with earlier Plinian fall deposits. An alternative possibility is that the welded pyroclastic block and ash flow deposits derive from a rapid series of gravitationally induced lava-dome-collapse-events that ultimately exhumed the hot interior of a large endogenously-supplied lava dome.

Welding reduces the total porosity in these block and ash flow deposits apparently by destroying both connected and isolated porosity (Fig. 10c). Fig. 13d (see inset) explores four possible paths for porosity reduction. Path 1 suggests that all Φ_I is reduced before any connected porosity is destroyed. This path might operate if fluids within isolated pores are resorbed into the host melt causing a local reduction in viscosity and facilitating compaction (*e.g.*, Sparks et al., 1999). Path 2 represents the reduction of all Φ_C prior to the destruction of Φ_I and would be favoured if fluid pressures within isolated pores are sufficient to counteract the compactional load pressures. Paths 3 and 4 allow for simultaneous destruction of Φ_C and Φ_I; path 3 maintains a constant ratio of connected and isolated porosity throughout compaction and goes through the origin. Path 4 appears to describe the Mount Meager dataset best; this path has a slope of 0.5 and allows for equal loss of Φ_C and Φ_I until all isolated porosity is removed.

7. Conclusion

The 2360 B.P. eruption of Mount Meager produced a sequence of block and ash pyroclastic flow deposits that form a 0.2–0.25 km^3 wedge-shaped deposit (Fig. 12b) filling the paleo–valley of the Lillooet River (Fig. 2a). The block and ash flow deposits are poorly sorted, unstructured, massive to weakly foliated, and variably welded. These deposits are unique in that they are densely welded, having transformed from unconsolidated material to vitroclastic obsidian.

Texture maps of outcrops (FTMs) provide a qualitative means of ranking welding intensity on the basis of flattening and re-orientation of clasts (Peterson, 1979); however, image analysis of these maps quantitatively underestimates the value of total compactional strain. Welding and compaction intensity are best tracked through changes in physical properties such as density and porosity. Welding is accommodated by compactional (volume) strain manifested by porosity reduction (both connected and isolated porosity) attending viscous deformation of clasts and matrix. Clasts and matrix record strain equally (~ 38%), and appear to be fully coupled during viscous deformation; strain is not localized preferentially into clasts as observed with welded ignimbrites.

Our reconstruction of the pre-welded deposit suggests a range of total porosity for juvenile rhyodacite clasts and matrix of 24–40% and 38–45%, respectively. Juvenile clasts can possess up to 8% isolated porosity, whereas all porosity in the matrix is connected. The average integrated strain, estimated from the extent of porosity reduction, is 31% for the thickest (112 m) portion of the sequence (Fig. 12); this suggests a minimum shortening of 50 m.

Porosity distributions found in the Mount Meager block and ash flow deposits support an explosive origin. Specifically, the presence of pervasive isolated porosity in the juvenile clasts of rhyodacite from the unwelded facies suggests that these block and ash flows were generated by the explosive collapse of hot domes and subsequent Vulcanian eruptions. An eruption analogue may include Soufrière Hills, where some characteristic block and ash flows are produced by Vulcanian eruptions that trigger explosive dome-collapse events.

Our preferred model for the origins of these deposits is block and ash pyroclastic flow deposits resulting from more or less continuous explosive collapse of young, hot rhyodacite lava domes. In the case of the 2360 B.P. eruption at Mount Meager, a rapidly produced succession of pyroclastic flows travelled a short distance (< 1 km) down the steep slopes of the volcanic edifice to be deposited in the Lillooet River valley (~ 2–3 km downstream). The welding of these deposits was facilitated by the hot, probably explosive, and sustained production of the block and ash flows and their containment within a steep, narrow canyon. In order to retain heat, the pyroclastic flows must have accumulated rapidly and must not have entrained much air as they traveled a short distance down the Lillooet River valley. The welding process was sufficiently intense that it transformed the majority of the originally unconsolidated deposit into a single cooling unit of dense, competent vitrophyre.

Acknowledgements

Research funds were provided by an NSERC CGS(M) scholarship (K. Michol) and a research grant from the NSERC Discovery grants program held by J.K. Russell. We are indebted to Willie Scott and an anonymous

referee for their careful and thoughtful reviews of the original manuscript.

Appendix A. FTM's and analysis of synthetic images

Results of image analysis for nine additional field texture maps that capture the full range of welding intensity are summarized in Fig. A1. Average values of oblateness from FTMs define the welding trajectory for these block and ash flow deposits (Fig. 8) but provide too low an estimate of total strain (*e.g.*,< 15%). Here, a qualitative empirical experiment is devised to help interpret the FTMs in terms of compactional strain. For demonstration purposes, a texture map from the basal non-welded facies (FTM 08; oblateness of 0.32) is used and digitally reduced in vertical dimension by 10, 20, 30, 40 and 50%. This digital shortening exactly parallels a volume (compactional) strain of 10–50% (Fig. A2). FTMs from the densely welded facies (FTM 05, 06) were then compared by eye to the digitally 'strained' images of FTM 08. The images of FTM 05 and 06 most closely resembled FTM 08 after a "*strain*" of 30–40%. This experiment and visual inspection of images implies that the densely welded facies have undergone 30–40% compactional strain, relative to the non-welded facies.

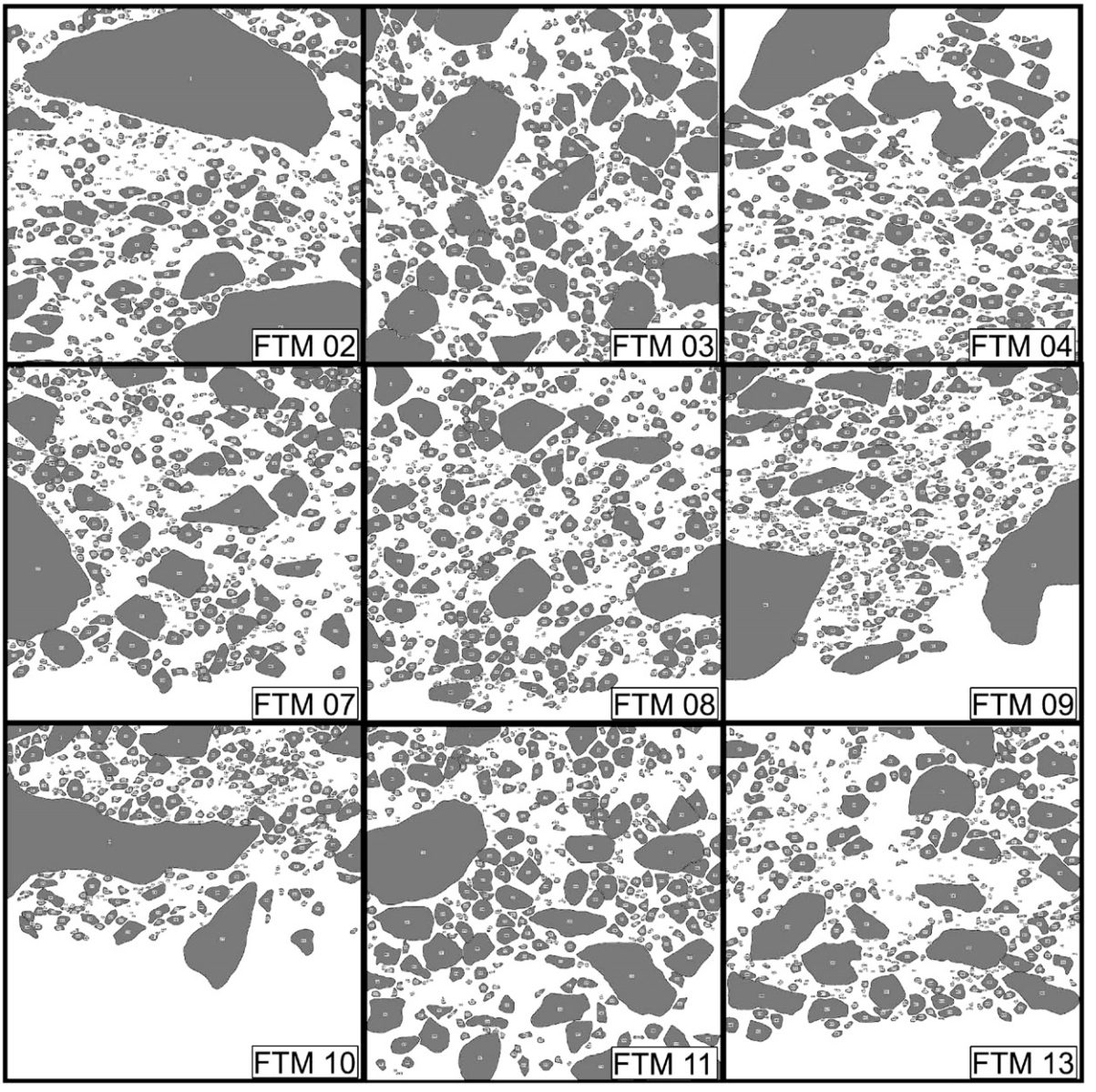

Fig. A1. Results of image analysis for nine additional Field Texture Maps (see text for discussion).

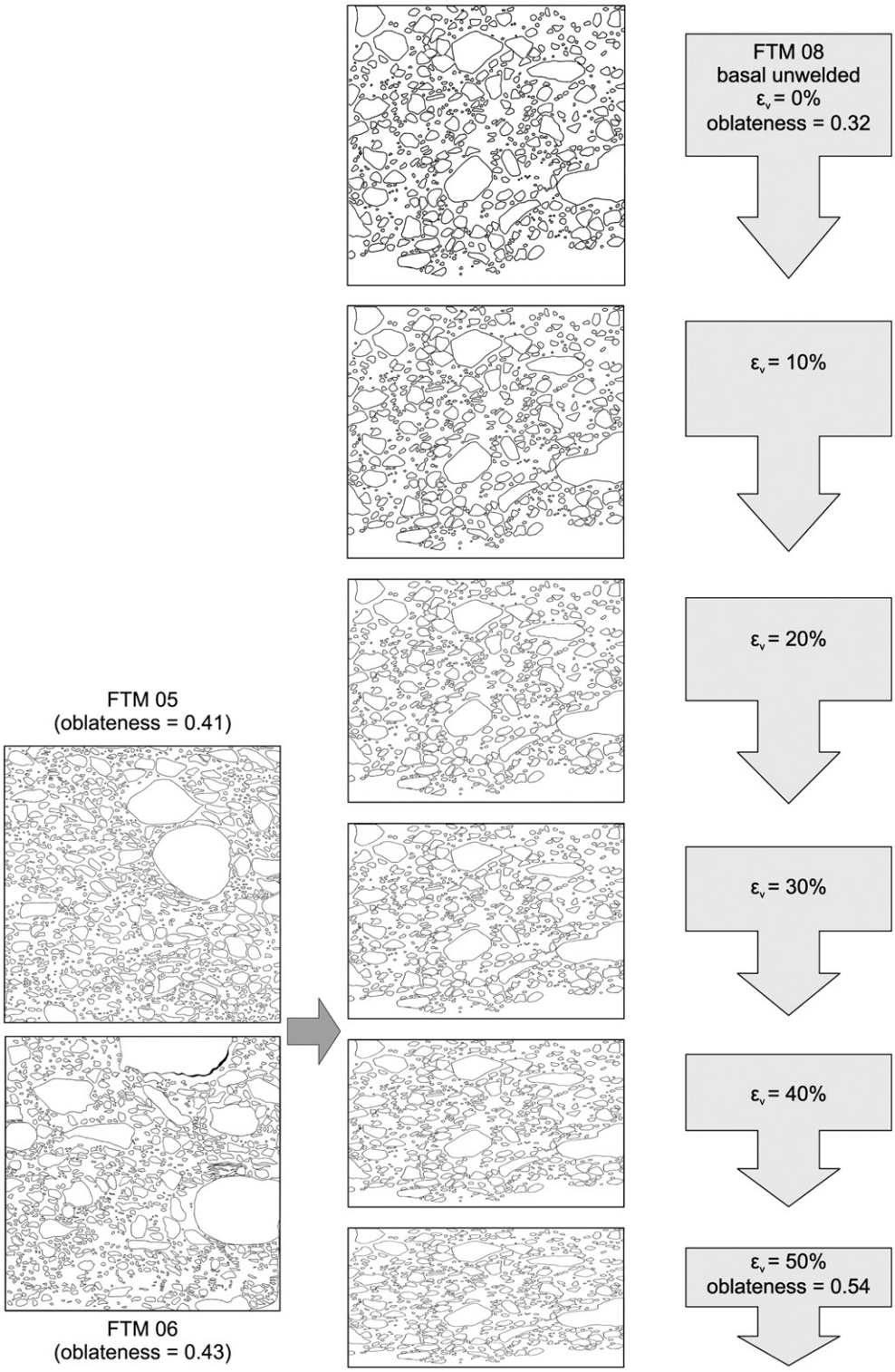

Fig. A2. Digital images produced from computer-simulated shortening of FTM 08. Images represent incremental shortenings of 10–50%. FTM 05 and 06 are displayed to show their similarity to FTM 08 after undergoing 30–40% synthetic compactional strain.

To complete our analysis we computed the average clast oblateness for the image produced when the image of FTM 08 was shortened by 50%. Scion Image analysis of the shortened image (Fig. A2) returns an average oblateness of 0.54. This value is lower than expected given the magnitude of total strain (50%) and the average clast oblateness in the original image (0.32). The implication is that 50% compactional strain induced a lower than expected increase in average oblateness (Δ=0.22 rather than 0.5). This provides corroboration for the lower-than-expected estimates of strain derived from the average values of oblateness from the FTMs.

Appendix B. Supplementary data

Supplementary data associated with this article can be found, in the online version, at doi:10.1016/j.jvolgeores.2007.08.010.

References

Abdurachman, E.K., Bourdier, J.-L., Voight, B., 2000. Nuées ardentes of 22 November 1994 at Merapi Volcano, Java, Indonesia. Journal of Volcanology and Geothermal Research 100, 345–361.

Bardintzeff, J.M., 1984. Merapi Volcano (Java, Indonesia) and Merapi-Type Nuée Ardente. Bulletin of Volcanology 47, 433–446.

Boudon, G., Camus, G., Gourgaud, A., Lajoie, J., 1993. The 1984 nuée-ardente deposits of Merapi volcano, Central Java, Indonesia: stratigraphy, textural characteristics, and transport mechanisms. Bulletin of Volcanology 55, 327–342.

Branney, M.J., Kokelaar, B.P., 2002. Pyroclastic density currents and the sedimentation of ignimbrites. Geological Society, London, Memoirs, vol. 27.

Calder, E.S., Luckett, R., Sparks, R.S.J., Voight, B., 2002. Mechanisms of lava dome instability and generation of rockfalls and pyroclastic flows at Soufrière Hills Volcano, Montserrat. In: Druitt, T.H., Kokelaar, B.P. (Eds.), The Eruption of Soufrière Hills Volcano, Montserrat, from 1995–1999. Geological Society of London, pp. 173–190.

Cas, R.A.F., Wright, J.V., 1987. Volcanic Successions; Modern and Ancient. Chapman and Hall, London. (528 p.).

Clague, J.J., Evans, S.G., Rampton, V.N., Woodsworth, G.J., 1995. Improved age estimates for White River and Bridge River tephras, western Canada. Canadian Journal of Earth Sciences 32, 1172–1179.

Cole, P.D., Calder, E.S., Sparks, R.S.J., Clarke, A.B., Druitt, T.H., Young, S.R., Herd, R.A., Harford, C.L., Norton, G.E., 2002. Deposits From Dome-Collapse And Fountain-Collapse Pyroclastic Flows At Soufrière Hills Volcano, Montserrat. In: Druitt, T.H., Kokelaar, B.P. (Eds.), The Eruption Of Soufrière Hills Volcano, Montserrat, From 1995–1999. Geological Society Of London, pp. 231–262.

Formenti, Y., Druitt, T.H., 2003. Vesicle connectivity in pyroclasts and implications for the fluidization of fountain-collapse pyroclastic flows, Montserrat (West Indies). Earth and Planetary Science Letters 214, 561–574.

Giordano, D., Dingwell, D.B., Romano, C., 2000. Viscosity of a Teide phonolite in the welding interval. Journal of Volcanology and Geothermal Research 103, 239–245.

Giordano, D., Nichols, A.R.L., Dingwell, D.B., 2005. Glass transition temperatures of natural hydrous melts: a relationship with shear viscosity and implications for the welding process. Journal of Volcanology and Geothermal Research 142, 105–118.

Green, N.L., Sinha, A.K., 2005. Consequences of varied slab age and thermal structure on enrichment processes in the sub-arc mantle of the northern Cascadia subduction system. Journal of Volcanology and Geothermal Research 140, 107–132.

Green, N.L., Armstrong, R.L., Harakal, J.E., Souther, J.G., Read, P.B., 1988. Eruptive history and K–Ar geochronology of the late Cenozoic Garabaldi volcanic belt, southwestern British Columbia. Geological Society of America Bulletin 100, 563–579.

Guest, J.E., Rogers, P.S., 1967. The sintering of glass and its relationship to welding in ignimbrites. Proceedings of the Geological Society of London 1641, 174–177.

Hickson, C.J., Russell, J.K., Stasiuk, M.V., 1999. Volcanology of the 2350 B.P. Eruption of Mount Meager Volcanic Complex, British Columbia, Canada: implications for hazards from eruptions in topographically complex terrain. Bulletin of Volcanology 60, 489–507.

Karatson, D., Sztano, O., Telbisz, T., 2002. Preferred clast orientation in volcaniclastic mass-flow deposits: application of a new photo-statistical method. Journal of Sedimentary Research 72 (6), 823–835.

Miyabuchi, Y., 1999. Deposits associated with the 1990–1995 eruption of Unzen volcano, Japan. Journal of Volcanology and Geothermal Research 89, 139–158.

Nasmith, H., Mathews, W.H., Rouse, G.E., 1967. Bridge River ash and some other recent ash beds in British Columbia. Canadian Journal of Earth Sciences 4, 163–170.

Peterson, D.W., 1979. Significance of the flattening of pumice fragments in ash flow tuffs. In: Chapin, C.E., Elston, W.E. (Eds.), Ash-flow tuffs. Geological Society of America, pp. 195–204.

Quane, S.L., Russell, J.K., 2005a. Ranking welding intensity in pyroclastic deposits. Bulletin of Volcanology 67, 129–143.

Quane, S.L., Russell, J.K., 2005b. Welding: insights from high-temperature analogue experiments. Journal of Volcanology and Geothermal Research 142, 67–87.

Quane, S.L., Russell, J.K., 2006. Bulk and particle strain analysis in high-temperature deformation experiments. Journal of Volcanology and Geothermal Research 154, 63–73.

Ragan, D.H., Sheridan, M.F., 1972. Compaction of the Bishop Tuff, California. Geological Society of America Bulletin 83, 95–106.

Read, P.B., 1977. Meager Creek volcanic complex, southwestern British Columbia. Report of Activities: Geological Survey of Canada Paper 77-1A, pp. 277–281.

Read, P.B., 1979. Geology of Meager Creek Geothermal Area, British Columbia. Geological Survey of Canada. Open File 603.

Read, P.B., 1990. Mount Meager Complex, Garibaldi Belt, Southwestern British Columbia. Geoscience Canada 17 (3), 167–170.

Riehle, J.R., Miller, T.F., Bailey, R.A., 1995. Cooling, degassing and compaction of rhyolitic ash-flow tuffs: a computational model. Bulletin of Volcanology 57, 319–336.

Ross, C.S., Smith, R.L., 1961. Ash-flow tuffs; their origin, geologic relations, and identification. U.S. Geological Survey Professional Paper 366 (81 pp.).

Russell, J.K., Quane, S.L., 2005. Rheology of welding: inversion of field constraints. Journal of Volcanology and Geothermal Research 142, 173–191.

Rust, A.R., Russell, J.K., Knight, R.J., 1999. Dielectric constant as a predictor of porosity in dry volcanic rocks. Journal of Volcanology and Geothermal Research 91, 79–96.

Sato, H., Fujii, T., Nakada, S., 1992. Crumbling of dacite dome lava and generations of pyroclastic flows at Unzen volcano. Nature 360, 664–666.

Sheridan, M.F., Ragan, D.H., 1976. Compaction of ash-flow tuffs. In: Chilingarian, G.V., Wolf, K.H. (Eds.), Compaction of Coarse-grained Sediments II. Elsevier, pp. 677–713.

Sherrod, D.R., Smith, J.G., 1990. Quaternary extrusion rates of the Cascade Range, northwestern United States and southern British Columbia. Journal of Geophysical Research 95, 19474–19645.

Smith, R.L., 1960a. Ash flows. Geological Society of America Bulletin 71 (6), 795–841.

Smith, R.L., 1960b. Zones and zonal variations in welded ash flows. U.S. Geological Survey Professional Paper 354-F, 149–159.

Sparks, R.S.J., Tait, S.R., Yanev, Y., 1999. Dense welding caused by volatile resorption. Journal of the Geological Society of London 156, 217–225.

Stasiuk, M.V., Russell, J.K., Hickson, C.J., 1996. Distribution, nature, and origins of the 2400 B.P. eruption products of Mount Meager, British Columbia: linkages between magma chemistry and eruption behaviour. Geological Survey of Canada Bulletin 486.

Stewart, M.L.2002. Dacite block and ash avalanche hazards in mountainous terrain: 2360 yr. B.P. eruption of Mount Meager, British Columbia. M.Sc. Thesis, The University of British Columbia.

Stewart, M.L., Russell, J.K., Hickson, C.J., 2003. Discrimination of hot versus cold avalanches: implications for hazard assessment at Mount Meager, B.C. Natural Hazards and Earth System Science, vol. 3, pp. 712–724.

Ui, T., Suzuki-Kamata, K., Matsusue, R., Fujita, K., Metsugi, H., Araki, M., 1989. Flow behavior of large-scale pyroclastic flows; evidence obtained from petrofabric analysis. Bulletin of Volcanology 51 (2), 115–122.

Ui, T., Matsuwo, N., Sumita, M., Fujinawa, A., 1999. Generation of block and ash flows during the 1990–1995 eruption of Unzen volcano, Japan. Journal of Volcanology and Geothermal Research 89, 123–137.

Wilson, C.J.N., Hildreth, W., 2003. Assembling an ignimbrite: mechanical and thermal building blocks in the Bishop Tuff, California. Journal of Geology 111, 653–670.

Woods, A.W., Sparks, R.S.J., Ritchie, L.J., Batey, J., Gladstone, C., Bursik, M.I., 2002. The explosive decompression of a pressurized volcanic dome: the 26 December 1997 collapse and explosion of Soufrière Hills Volcano, Montserrat. In: Druitt, T.H., Kokelaar, B.P. (Eds.), The Eruption of Soufrière Hills Volcano, Montserrat, from 1995–1999. Geological Society of London, pp. 457–465.

Wright, H., Cashman, K.V., Rosi, M., Cioni, R., 2007. Breadcrust bombs as indicators of Vulcanian eruption dynamics at Guagua Pichincha volcano, Ecuador. Bulletin of Volcanology 69 (3), 281–300.